nature nanotechnology

ARTICLES

https://doi.org/10.1038/s41565-022-01151-y

Check for updates

Kinetic and energetic insights into the dissipative non-equilibrium operation of an autonomous light-powered supramolecular pump

Stefano Corra[1,2,6], Marina Tranfić Bakić[1,2,6], Jessica Groppi[1], Massimo Baroncini[1,3], Serena Silvi[1,4], Emanuele Penocchio[5], Massimiliano Esposito[5] and Alberto Credi[1,2] ✉

Natural and artificial autonomous molecular machines operate by constantly dissipating energy coming from an external source to maintain a non-equilibrium state. Quantitative thermodynamic characterization of these dissipative states is highly challenging as they exist only as long as energy is provided. Here we report on the detailed physicochemical characterization of the dissipative operation of a supramolecular pump. The pump transduces light energy into chemical energy by bringing self-assembly reactions to non-equilibrium steady states. The composition of the system under light irradiation was followed in real time by ^{1}H NMR for four different irradiation intensities. The experimental composition and photon flow were then fed into a theoretical model describing the non-equilibrium dissipation and the energy storage at the steady state. We quantitatively probed the relationship between the light energy input and the deviation of the dissipative state from thermodynamic equilibrium in this artificial system. Our results provide a testing ground for newly developed theoretical models for photoactivated artificial molecular machines operating away from thermodynamic equilibrium.

Natural and artificial molecular machines, such as molecular motors and pumps, can be rationally described as networks of reactions where energy-harvesting chemical[1–10] or photochemical[11–20] reactions are coupled with large-amplitude intramolecular motions or self-assembly processes that can be driven towards a non-equilibrium state (Fig. 1a)[21–26].

The determination of the speciation in the out-of-equilibrium state is highly desirable, as several thermodynamic and kinetic parameters of the machine operation could be extracted. However, the characterization of dissipative states is extremely challenging as it requires any analysis to be performed during operation, that is in the presence of the fuel-to-waste conversion[27–29].

We recently reported on a series of light-powered molecular motors based on a pseudorotaxane-complex architecture. The operational principle relies on the reversible photoisomerization of the azobenzene moiety of the axle which enables a flashing energy ratchet mechanism (Fig. 1b). As the system realizes linear-directed transport of one molecular component relative to another, as a result of the Brownian ratchet mechanism, we refer to it as a supramolecular pump. Under continuous irradiation, the crown ether macrocycle undergoes autonomous and directional cycling between the assembled and disassembled states[21,30,31]. In the setup described here, our pump operates 'freewheel' and, unlike other systems[8–10], it cannot build up a concentration gradient. Nonetheless, its dissipative operation as a molecular motor was proved by comparing the thermodynamic and kinetic data for the two—*E* and *Z*—isomers, as well as by ^{1}H NMR while irradiating the sample solution inside the NMR probehead[30–32]. Specifically, this technique allows for the real-time monitoring of the system composition at the dissipative steady state. Building upon these results, we focused here on the physicochemical characterization of the operation cycle and dissipative steady state of a previously reported supramolecular pump. The cycling rate, quantum yield, energy storage and power conversion efficiency were derived from the experimental concentrations at different incident photon flows. Moreover, we probed a relationship between the light energy input and the deviation of the dissipative state from the equilibrium composition in this artificial system.

Structure and operation of the supramolecular pump

The supramolecular pump is composed of a dibenzo[24]crown-8 (DB24C8) ether macrocycle (**1**) and a molecular axle (**2**$^+$), which comprises a secondary ammonium recognition site for **1** flanked by a photoswitchable azobenzene gate and a cyclopentyl 'pseudostopper' (Fig. 1c). Briefly, in acetonitrile the macrocycle encircles the secondary ammonium station of the axle to form a stable hydrogen-bonded rotaxane-type complex for both the *E* and *Z* isomers of **2**$^+$. The *E* complex is slightly more stable than the *Z* complex ($K_a^E > K_a^Z$) and its formation occurs almost exclusively by slippage of the ring over the *E*-azobenzene moiety (Table 1). The non-photoactive pseudostopper was selected to ensure that the formation of the *Z* complex occurred almost exclusively by slippage of the ring over the cyclopentyl moiety[30,31].

The $E \rightarrow Z$ isomerization of the axle has, therefore, two key consequences: (1) the destabilization of the threaded complex and (2) the increase of the activation energy for the slippage of the ring over the azobenzene extremity[30,31,33]. As a result, light-induced unidirectional transport of the rings over the pump occurs according to an energy ratchet mechanism (Fig. 1b). As both *E* and *Z* isomers of azobenzene are photoreactive and exhibit highly overlapped absorption spectra, photons of the same wavelength can trigger both $E \rightarrow Z$ and

[1]CLAN-Center for Light Activated Nanostructures, Istituto ISOF-CNR, Bologna, Italy. [2]Dipartimento di Chimica Industriale 'Toso Montanari', Università di Bologna, Bologna, Italy. [3]Dipartimento di Scienze e Tecnologie Agro-alimentari, Università di Bologna, Bologna, Italy. [4]Dipartimento di Chimica 'G. Ciamician', Università di Bologna, Bologna, Italy. [5]Department of Physics and Materials Science, University of Luxembourg, Luxembourg City, Luxembourg. [6]These authors contributed equally: Stefano Corra, Marina Tranfić Bakić. ✉e-mail: alberto.credi@unibo.it

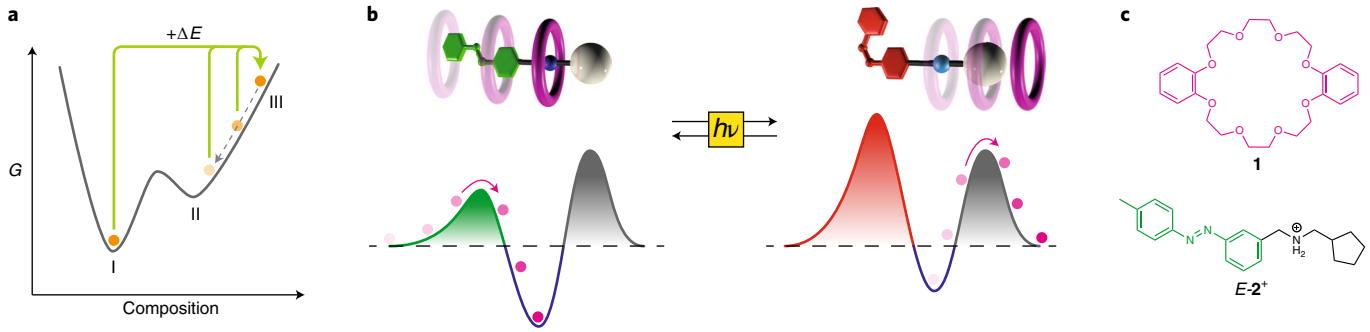

Fig. 1 | Simplified energy diagrams of operation of the pump and molecular structures of the components. a, Idealized landscape of the total Gibbs free energy (*G*) of a chemical system, showing the global thermodynamic minimum that corresponds to the thermal equilibrium (I), a local equilibrium state (II) and a dissipative non-equilibrium state (III). State III exists only if energy is continuously supplied to the system (solid green arrows) to prevent its relaxation to state II (dashed grey arrow). **b**, Schematic representation of the relative unidirectional translation of molecular ring and axle components triggered by light, that is, a supramolecular pump powered by light. The simplified potential energy curves (free energy versus ring–axle distance) corresponding to the two structures illustrate the energy ratchet mechanism that rectifies the Brownian motion of the ring. **c**, Molecular structure of the components of the supramolecular pump of the present study: the DB24C8 macrocycle **1** and the non-symmetric molecular axle *E*-**2**$^+$.

$Z \rightarrow E$ isomerization. The system is, thus, able to repeat the cycle autonomously under constant illumination, reaching and maintaining a stationary non-equilibrium state dissipating light energy.

The operation of the molecular pump can be described with the reaction network depicted in Fig. 2. Two thermal processes (self-assembly, numbered 1 and 3, following mass-action kinetics) and two photochemical processes (*E*/*Z* isomerization, numbered 2 and 4, following nonlinearized photokinetics) are involved in the cycle. Only the two thermal processes must satisfy microscopic reversibility, as photochemical processes result from reaction mechanisms involving excited states of the molecules[34–37]. Since the photoisomerization quantum yields and molar absorption coefficients of the free and complexed axle are almost identical (Supplementary Table 2), they exhibit essentially the same *E*/*Z* composition at the photostationary state (PSS), that is $K^{u}_{h\nu} = K^{c}_{h\nu}$. Conversely, the equilibrium constants for the self-assembly processes are different, specifically $K^{E}_{a} > K^{Z}_{a}$ (ref. [30,31]). As a consequence, under irradiation, detailed balance in this reaction network cannot be fulfilled and the cycle is travelled clockwise with a non-zero net rate[31,38]. The ability of the system to cycle preferentially clockwise with respect to anticlockwise—that is, its kinetic asymmetry—is quantified by the ratcheting constant (K_r), defined as the ratio between the clockwise and anticlockwise rates[39,40]. For our system under irradiation, K_r is well approximated by the ratio $K^{E}_{a}/K^{Z}_{a} = 2$ meaning that, on average, the system loops anticlockwise once every two cycles in the clockwise direction (Supplementary Section 3.3).

Study of the light-dependent dissipative regime

A typical feature of dissipative systems is that a fraction of the energy input is employed to shift concentrations away from equilibrium values and is, thus, stored as free energy into the system[3,19,41,42]. In fact, in a closed cycle of reactions when detailed balance is not fulfilled, the cycling net rate must be equal for all steps and non-zero ($v_{cy} \equiv v_1 = v_2 = -v_3 = -v_4 \neq 0$)[34]. To satisfy this condition, the concentration of the species under operation must adjust to a level which is different from that of equilibrium. This is exactly what is observed for the cycle of the supramolecular pump (Fig. 2a)[31].

Since the rates of the individual photochemical reactions (v_2 and v_4) are dictated by the photon flow (Fig. 2b), variation of the latter will modify the overall cycling rate. Therefore, the self-assembly steps (1 and 3) must adapt their net rate of reaction to the new cycling rate, adjusting the concentration of reagents and products to a different level. As a consequence, for reactions (1) and (3) a larger deviation from the equilibrium concentrations is expected at a higher photon flow. In turn, this means that, also in a light-driven system, the amount of stored energy should be correlated to the amount of energy provided by the external reservoir[37,41].

Table 1 | Thermodynamic and kinetic parameters[a] in air-equilibrated CD_3CN at 298 K for the rotaxane-type complexes formed between 1 and either *E*-2$^+$ or *Z*-2$^+$

	K_a (mol l^{-1})[b]	k_{in} (l mol^{-1} s^{-1})[c]	k_{out} (s^{-1})[d]
1 + *E*-**2**$^+$	230 ± 30	16 ± 3[e]	0.07[f]
1 + *Z*-**2**$^+$	115 ± 35[g]	(3.1 ± 0.8) × 10^{-2} [h]	(2.7 ± 0.5) × 10^{-4} [h]

[a]From ref. [30]. [b]Association constant. [c]Threading rate constant. [d]Dethreading rate constant. [e]Determined by stopped-flow ultraviolet–visible absorption method. [f]Calculated as k_{in}/K_a. [g]Calculated as k_{in}/k_{out}. [h]Determined from time-dependent ^{1}H NMR concentration profiles.

To probe this hypothesis it is crucial to measure the speciation in real time upon operation of the pump. In situ irradiation in the NMR probehead, as demonstrated recently, is perfectly suited for this task[31,32]. We employed an optical fibre to deliver nearly monochromatic ultraviolet light ($\lambda_{irr} = 365 \pm 5$ nm) to the solution inside the NMR tube (Supplementary Fig. 2). The monochromatic setup is advantageous because (1) the behaviour of the system can be appropriately described using spectroscopic and photochemical parameters independently measured for the pump components (Supplementary Table 2) and (2) the photon flow can be accurately determined by chemical actinometry. Both these points are fundamental to perform quantitative numerical simulations to support the pump operating cycle.

Typically, an equimolar mixture of *E*-**2**$^+$ and **1** (8.9 mM) was equilibrated in the dark and then irradiated with full-power 365 nm light (photon flow, 4.4×10^{-8} Einstein s^{-1}) until a constant *Z*/*E* composition was reached (35 min). During this time, the *E*-configured axle and complex were photoconverted into the corresponding *Z* species faster than the disassembly of the *Z* complex. Thus, the *Z* species were produced in relative concentrations that were not consistent with K^{Z}_{a}; specifically, the *Z* complex was kinetically trapped in a concentration higher than its equilibrium value. In the first instance, after reaching the PSS, the irradiation was turned off and spectra were acquired over time. In the dark, a decrease in the concentration of the *Z* complex, accompanied by a corresponding increase in the concentration of *Z* axle, was observed,

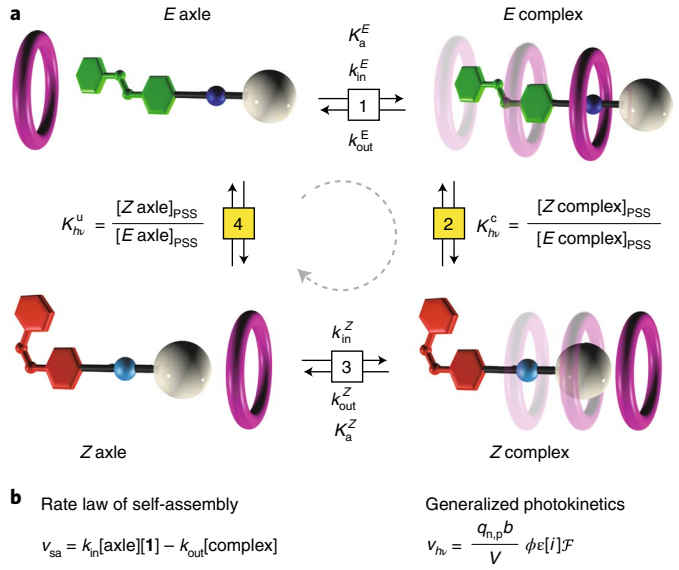

Fig. 2 | Operative reaction network of the supramolecular pump. **a**, Thermal self-assembly equilibria (1 and 3) and photochemical isomerization reactions (2 and 4). The fictitious 'equilibrium constants' for the photochemical steps are defined as the ratio of the concentrations of the products and reactants at the PSS for the respective reactions. The dashed circular arrow indicates the net direction of travelling of the cycle. Conventionally all the parameters are positive for the reactions read from left to right and from top to bottom. **b**, Left: general rate law for the self-assembly reactions (1 and 3) following mass-action kinetics. Right: generalized photokinetics for photochemical reactions (2 and 4). $q_{n,p}$, photon flow; ϕ; quantum yield; ε, molar absorption coefficient; $\mathcal{F}$, photokinetic factor; i, photoactive species; b, optical path; V, volume of irradiated solution.

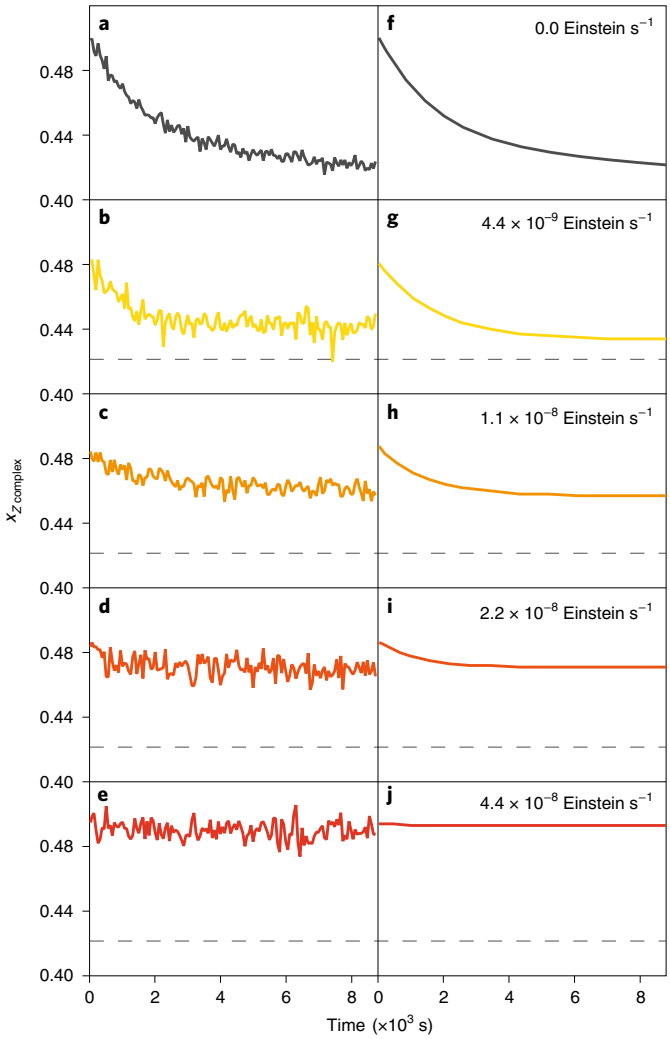

Fig. 3 | Time-dependent concentration profiles of complexed *Z*-2^{+}. **a**–**j**, Experimental (left) and simulated (right) molar fraction profiles after photogeneration of the kinetically trapped *Z* complex in the dark (**a**,**f**) and upon constant irradiation at 365 nm with different light intensities (**b**–**e** and **g**–**j**). The photon flow employed to maintain the dissipative state is indicated on the right-hand side of each panel. The dashed lines mark the molar fraction of the *Z* complex at the local equilibrium in the dark corresponding to the plateau of the curve in **a**. Conditions: CD_3CN, 298 K, [**1**] = [**2**$^{+}$] (initial concentrations for each experiment are reported in Supplementary Table 2).

as **1** dethreaded to satisfy the equilibrium condition. After about 2 h (local) equilibrium was reached with a decrease in the *Z* complex concentration of about 10% (Fig. 3a). It should be noted that the *Z* species are kinetically trapped with respect to azobenzene isomerization because the thermodynamically stable isomer is *E*. For the sake of simplicity, from this point onward we shall refer to the kinetically trapped state of the system as an 'equilibrium state' referring to the local equilibrium of the *Z* complex self-assembly reaction. It has to be made clear, though, that the true equilibrium state of our system is the absence of *Z* species. It is also important to note that the thermal $Z \rightarrow E$ isomerization during this interval was negligible.

In the second instance, after reaching the PSS the irradiation was continued with the same photon flow (4.4×10^{-8} Einstein s^{-1}), or with a flow attenuated to 50%, 25% or 10% of the initial value (Supplementary Fig. 2). In all cases, new PSSs were reached within about 1 h in which the concentration of the *Z* complex was higher than the value reached in the dark (Fig. 3b–e). On the other hand, the concentration of the *Z* axle was lower than that in the dark (Supplementary Fig. 4). These results confirm that the system reached a dissipative non-equilibrium steady state in which the *Z* complex was kinetically accumulated at the expense of the *Z* axle[31]. The concentrations of the *Z* complex and *Z* axle progressively deviated more from their equilibrium values upon increasing the photon flow. Hence, we can qualitatively conclude that a larger energy input—more photons per unit time—drives the system farther away from equilibrium.

Numerical simulations, performed using experimentally determined (photo)chemical and photophysical parameters, provided time-dependent concentration profiles for all species. It is noteworthy that in the simulations the concentrations were assumed to be homogeneous in space. This assumption is not obvious a priori, as the intensity of the photon flux is dependent on the radius of the NMR tube. Nonetheless, the concentration profiles are in excellent agreement with the experimental data (Fig. 3f–j and Supplementary Fig. 4), confirming the fast diffusion of the molecules with respect to the cycling time of the pump. Moreover, the simulated data also confirm that the disassembly of the *Z* complex acts as the bottleneck for the reaction network. Thus, the *Z* complex is kinetically accumulated in different amounts depending on the intensity of the incident light.

Kinetic and energetic considerations

The possibility to directly measure or estimate by means of simulations the concentration of the species at the dissipative steady state provided us the unprecedented opportunity to gain quantitative

Table 2 | Kinetic and energetic parameters of the cycle of the 1/2^{+} ensemble for dissipative non-equilibrium operation under different photon flows[a]

q_p (Einstein s^{-1})[b]	v_3 (μM s^{-1})[c]	Φ_{cy} [$N_{h\nu}$ per cycle][d]	$\Delta\mu_1$ (J mol^{-1})[e]	$\Delta\mu_3$ (J mol^{-1})[e]	$T\Delta_{cy\ sa}$ (J mol^{-1})[f]	ΔG_{sa} (J l^{1})[g]	η (%)[h]
0	-	-	0	0	0	0	-
4.4×10^{-9}	−0.25	0.11 [9]	−40	1,380	1,420	0.25	0.3
1.1×10^{-8}	−0.34	0.06 [16]	−64	1,776	1,840	0.48	0.2
2.2×10^{-8}	−0.38	0.04 [28]	−89	1,961	2,050	0.61	0.1
4.4×10^{-8}	−0.42	0.02 [53]	−149	1,902	2,051	0.63	0.08

[a]Conditions: CD_3CN, 298 K, [**1**] = [**2**$^{+}$] (initial concentrations for each experiment are reported in Supplementary Table 2), λ_{irr} = 365 nm. All the properties refer to the whole system with homogeneous (well-mixed) concentrations. [b]Photon flow at 365 nm, determined by chemical actinometry. [c]Rate of reaction (3) at the stationary state calculated according to equation (1); see Fig. 2 for the sign convention. [d]Quantum yield of the cycle calculated using Supplementary equation (S2); numbers in brackets are the number of absorbed photons per cycle ($1/\Phi_{cy}$). [e]Chemical potential of reaction according to Supplementary equation (S9), determined from simulated (reaction (1)) or experimental (reaction (3)) concentration values. [f]Free energy dissipated by self-assembly steps during a cycle of operation at the steady state. [g]Free energy density stored in the self-assembly steps at the non-equilibrium steady state. [h]Energy transduction efficiency, calculated as the ratio between $T\Delta_{cy}\Sigma_{sa}$ and the total amount of free energy absorbed during a cycle of operation at the steady state.

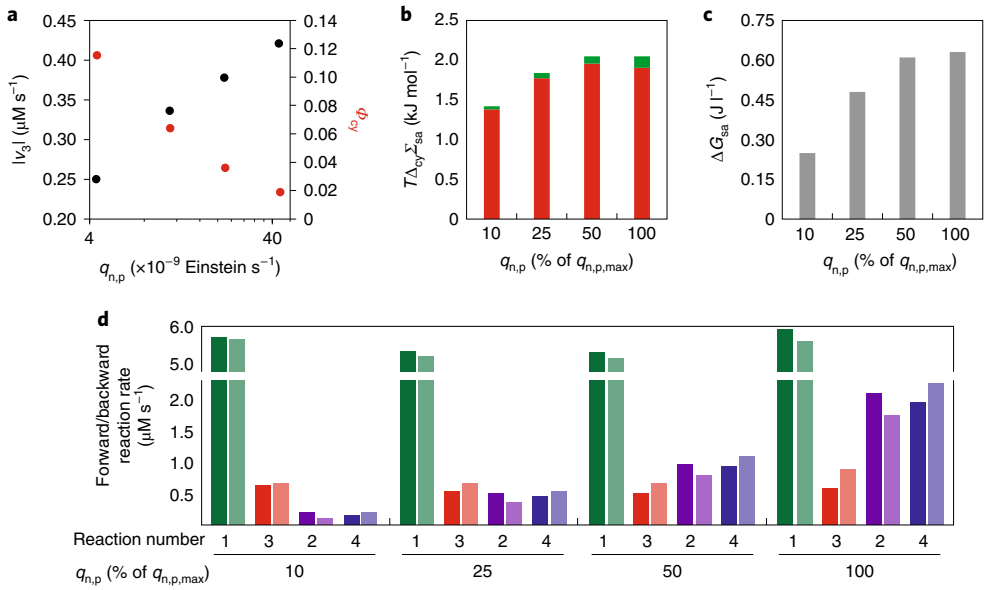

Fig. 4 | Dependence of the kinetic and thermodynamic parameters on the photon flow. a, Net cycling rate (black dots) and quantum yield of cycling (red dots) at 298 K. **b**, Free energy dissipated by the self-assembly steps during one cycle of operation at the steady state. The fractions of free energy dissipated by reactions (1) (green bars) and (3) (red bars) are indicated. **c**, Free energy density stored in the self-assembly steps. **d**, Simulated forward (dark bars) and backward (light bars) rates for reactions (1) (green), (2) (purple), (3) (red) and (4) (blue) at different photon flows. In the bar graphs the photon flow is expressed as a percentage of the maximum flow ($q_{n,p,max} = 4.4\times10^{-8}$ Einstein s^{-1} = 100%).

information on the reaction network under autonomous cycling away from equilibrium.

The first quantity that can be extracted from our data is the rate of cycling under irradiation. As discussed above, in a closed cycle of reactions, at the steady state, all the reactions must proceed at the same net rate. Therefore, the rate of cycling at the steady state can be calculated on any reaction of the network (Fig. 2). The rate of reaction (3) (v_3) was calculated using a mixed-order kinetic equation (equation (1)) from the experimental concentrations at the steady state and the rate constants (Table 2).

$$v_3 = k^{Z}_{in}\,[Z\,\text{axle}]\,[1] - k^{Z}_{out}\,[Z\,\text{complex}] \equiv -v_{cy} \qquad (1)$$

The rate v_3 is negative for all photon flows, indicating that the Z complex is undergoing dethreading and that the cycle shown in Fig. 2 is being travelled clockwise (dashed circular arrow), consistent with previous considerations on the kinetic asymmetry. As anticipated, the cycling rate (v_{cy}) becomes larger upon increasing the photon flow (Table 2 and Fig. 4a). Finally, the K_r of the system, calculated from the simulated clockwise and anticlockwise reaction rates, is close to the estimated value of 2 (Supplementary Table 3).

On the contrary, the quantum yield of the cycle (Φ_{cy}, Table 2), that is the number of molecules that have completed a full cycle upon the absorption of one photon, decreases from 11% at the lowest photon flow to 2% at the highest photon flow (Fig. 4a). This means that, on average at the lowest light intensity, a given ring/axle pair needs to absorb nine photons to complete a cycle, while this number becomes more than five times larger at the highest intensity (Table 2).

The chemical potential difference ($\Delta\mu$) of each process at the steady state can be directly calculated from the experimental or simulated concentrations (Supplementary Section 5.1) and can be interpreted as a measure of how far the reaction is from equilibrium[43]. The steady state $\Delta\mu$ values of the self-assembly of the E (reaction (1), $\Delta\mu_1$) and the Z (reaction (3), $\Delta\mu_3$) complexes both increase in magnitude upon increasing the photon flow (Table 2).

This means that both reactions are progressively displaced farther from their equilibrium state; however, they exhibit opposite trends. Specifically, $\Delta\mu_3$ becomes more positive upon increasing the photon flow, showing that larger light intensities drive reaction (3) more towards the product. Such an observation is consistent with the kinetic accumulation of the Z complex and with the increasingly negative values of v_3. Conversely, $\Delta\mu_1$ becomes more negative at higher light intensities, indicating that reaction (1) is progressively shifted back towards the reagents. Therefore, at the steady state the Z complex and E axle are accumulated, whereas the E complex and Z axle are depleted due to purely kinetic effects[44].

From a thermodynamic point of view, our system can be thought of as a thermal machine powered by the gradient between the temperature T of the solvent (the cold reservoir) and the temperature $T_{h\nu}$ of the radiation (the hot reservoir), which can be correlated to the experimental photon flow using Planck's law (Supplementary Section 5.2). As a consequence, its efficiency is limited by Carnot's theorem[35,36]. The gradient of temperature powering the machine also relates to the chemical potential gradient generated by the radiation (Supplementary Table 7). Larger photon flows correspond to a higher temperature of the hot reservoir, thus producing a larger free energy gradient to drive the machine farther away from equilibrium[35–37,45]. In the present case, the gradient is about one order of magnitude higher than that delivered by the hydrolysis of adenosine triphosphate (ATP) in physiological conditions and comparable to that generated by, for example, the decarboxylation of the fluorenylmethoxycarbonyl group employed to power other synthetic molecular motors[12].

Each time a photon is absorbed by the system, its free energy can be either dissipated or converted into chemical free energy by changing the concentration distribution[37,41,43,46]. This can be expressed with the following instantaneous free energy balance:

$$\dot{W}_{h\nu} = d_t G + T\dot{\Sigma} \quad (2)$$

where $\dot{W}_{h\nu}$, $d_t G$ and $T\dot{\Sigma}$ are the free energy densities absorbed, stored and dissipated, respectively, by the whole system per unit time. By integrating equation (2) it is possible to compute the amount of free energy dissipated and stored in any time interval (Supplementary Section 5.3).

When the system reaches the steady state, the power absorbed from the radiation is no longer stored in the system ($d_t G = 0$), but is entirely dissipated to sustain the non-equilibrium steady state[46]. Thus, over one cycle, $\Delta_{cy} W_{h\nu} = T\Delta_{cy}\Sigma$. This free energy dissipation can be split into two contributions: that of the self-assembly and that of the isomerization processes, namely $T\Delta_{cy}\Sigma = T\Delta_{cy}\Sigma_{sa} + T\Delta_{cy}\Sigma_{iso}$ (ref. [47]). The self-assembly dissipation ($T\Delta_{cy}\Sigma_{sa}$) is the portion of the absorbed free energy responsible for keeping the self-assembly steps out of equilibrium and for sustaining the unidirectional motion of the rings with respect to the axles. This value can also be calculated from $\Delta\mu_1$ and $\Delta\mu_3$ (Supplementary Section 5.3.1). Dissipation increases with the photon flow (Table 2), consistently with the self-assembly steps being progressively shifted away from their equilibrium state. The fraction of free energy input dissipated by the self-assembly reactions is the efficiency of free energy transduction from the photo-isomerization processes towards the self-assembly ones ($\eta = T\Delta_{cy}\Sigma_{sa}/\Delta_{cy} W_{h\nu}$)[47]. The efficiency is relatively small at all operating regimes, meaning that most of the free energy harvested from the radiation is dissipated by the photoisomerization steps.

The free energy density stored in the self-assembly steps (ΔG_{sa}) coincides with the difference between the Gibbs free energy densities in the steady and local equilibrium states ($\Delta G_{sa} = G_{light} - G_{dark}$, see Supplementary Section 5.3.2). Thus, it can be computed from the experimentally determined steady state concentrations. It is noteworthy that the free energy storage increases with the photon flow until it reaches a plateau around 0.6 J l^{-1}.

Interestingly, two distinct trends can be identified in the dependence of the determined quantities on the light intensity. Upon increasing the photon flow, ΔG_{sa}, $T\Delta_{cy}\Sigma_{sa}$ and v_{cy} increase, reaching a plateau between 1 and 2×10^{-8} Einstein s^{-1}, while η and Φ_{cy} decrease (Fig. 4a–c). This observation is in qualitative agreement with the results of stochastic simulations performed on a closely related molecular pump, which predicted that the network can process photons efficiently only as long as the photoreactions are the rate-limiting steps[48]. To support this claim, we compared the forward and backward rates of each reaction in the network (Fig. 4d). At the steady state, the forward and backward reaction rates (Fig. 4d) can assume different values for the four processes, provided that their relative difference is the same for all reactions. In fact, for photon flows up to 1.1×10^{-8} Einstein s^{-1} (that is, 25% of $q_{n,p,max}$), the photochemical reactions are slower than the thermal ones and determine the overall cycling rate in either direction. Conversely, at higher flows reaction (3) becomes rate limiting (red bars in Fig. 4d), while photoreactions proceed faster dissipating a larger fraction of light energy, thus reducing the energy transduction efficiency.

The observed decrease of the quantum yield of the cycle (Φ_{cy}) (Table 2) is also coherent with this picture. Notably, already at the lowest flow employed, completing one cycle requires nine photons (Table 2), a number significantly larger than the theoretical minimum value of two. This means that, in the investigated light intensity range, a given axle (complex) undergoes several $E \leftrightarrows Z$ photoisomerization events before threading (dethreading). Increasing the rate of the photoreactions increases the number of unfruitful $E \leftrightarrows Z$ isomerization events. As indicated by earlier simulations[48], only at low photon rates can the pump operate close to the maximum quantum efficiency.

Conclusions

A combination of experimental data and numerical simulations was used to characterize from a kinetic and thermodynamic point of view the dissipative photostationary states of a supramolecular pump for four intensities of incident light. Our measurements quantitatively probed the relationship between the deviation from thermodynamic equilibrium and the photon flow and provide an unprecedented insight in the non-equilibrium behaviour of (photo) chemical reaction networks. Although in the current design the stored energy cannot be converted into work, our analysis allows the maximum amount of free energy which can potentially be converted into work to be quantified. We believe that this approach is applicable to investigate any kind of light-fuelled non-equilibrium chemical ensemble, providing a testing ground for recently developed theoretical models[27]. We envision that our results will stimulate research on new, more sophisticated light-driven artificial molecular machines and materials capable of operating away from thermodynamic equilibrium.

Online content

Any methods, additional references, Nature Research reporting summaries, source data, extended data, supplementary information, acknowledgements, peer review information; details of author contributions and competing interests; and statements of data and code availability are available at https://doi.org/10.1038/s41565-022-01151-y.

Received: 23 December 2021; Accepted: 12 May 2022;
Published online: 27 June 2022

References

1. Schliwa, M. & Woehlke, G. Molecular motors. *Nature* **422**, 759–765 (2003).
2. Goodsell, D. S. *The Machinery of Life* (Copernicus, 2009).
3. Solis Muñana, P. et al. Substrate-induced self-assembly of cooperative catalysts. *Angew. Chem. Int. Ed.* **57**, 16469–16474 (2018).

4. Yang, S. et al. Chemical fueling enables molecular complexification of self-replicators. *Angew. Chem. Int. Ed.* **60**, 11344–11349 (2021).
5. Boekhoven, J. et al. Dissipative self-assembly of a molecular gelator by using a chemical fuel. *Angew. Chem. Int. Ed.* **49**, 4825–4828 (2010).
6. Wilson, M. R. et al. An autonomous chemically fueled small-molecule motor. *Nature* **534**, 235–240 (2016).
7. Borsley, S., Kreidt, E., Leigh, D. A. & Robert, B. M. W. Autonomous fuelled directional rotation about a covalent single bond. *Nature* **604**, 80–85 (2022).
8. Amano, S., Fielden, S. D. P. & Leigh, D. A. A catalysis-driven artificial molecular pump. *Nature* **594**, 529–534 (2021).
9. Cheng, C. et al. An artificial molecular pump. *Nat. Nanotechnol.* **10**, 547–553 (2015).
10. Qiu, Y. et al. A precise polyrotaxane synthesizer. *Science* **368**, 1247–1253 (2020).
11. Astumian, R. D. Optical vs. chemical driving for molecular machines. *Faraday Discuss.* **195**, 583–597 (2016).
12. Kathan, M. & Hecht, S. Photoswitchable molecules as key ingredients to drive systems away from the global thermodynamic minimum. *Chem. Soc. Rev.* **46**, 5536–5550 (2017).
13. Baroncini, M., Silvi, S. & Credi, A. Photo- and redox-driven artificial molecular motors. *Chem. Rev.* **120**, 200–268 (2020).
14. Feringa, B. L. The art of building small: from molecular switches to motors (Nobel Lecture). *Angew. Chem. Int. Ed.* **56**, 11060–11078 (2017).
15. Ragazzon, G., Baroncini, M., Silvi, S., Venturi, M. & Credi, A. Light-powered autonomous and directional molecular motion of a dissipative self-assembling system. *Nat. Nanotechnol.* **10**, 70–75 (2015).
16. Ceroni, P., Credi, A. & Venturi, M. Light to investigate (read) and operate (write) molecular devices and machines. *Chem. Soc. Rev.* **43**, 4068–4083 (2014).
17. Foy, J. T. et al. Dual-light control of nanomachines that integrate motor and modulator subunits. *Nat. Nanotechnol.* **12**, 540–545 (2017).
18. Ikegami, T., Kageyama, Y., Obara, K. & Takeda, S. Dissipative and autonomous square-wave self-oscillation of a macroscopic hybrid self-assembly under continuous light irradiation. *Angew. Chem. Int. Ed.* **55**, 8239–8243 (2016).
19. Herder, M. & Lehn, J.-M. The photodynamic covalent bond: sensitized alkoxyamines as a tool to shift reaction networks out-of-equilibrium using light energy. *J. Am. Chem. Soc.* **140**, 7647–7657 (2018).
20. Greb, L., Eichhçfer, A. & Lehn, J.-M. Synthetic molecular motors: thermal N inversion and directional photoinduced C=N bond rotation of camphorquinone imines. *Angew. Chem. Int. Ed.* **54**, 14345–14348 (2015).
21. Cheng, C., McGonigal, P. R., Stoddart, J. F. & Astumian, R. D. Design and synthesis of nonequilibrium systems. *ACS Nano* **9**, 8672–8688 (2015).
22. Merindol, R. & Walther, A. Materials learning from life: concepts for active, adaptive and autonomous molecular systems. *Chem. Soc. Rev.* **46**, 5588–5619 (2017).
23. Ragazzon, G. & Prins, L. J. Energy consumption in chemical fuel-driven self-assembly. *Nat. Nanotechnol.* **13**, 882–889 (2018).
24. van Rossum, S. A. P., Tena-Solsona, M., van Esch, J. H., Eelkema, R. & Boekhoven, J. Dissipative out-of-equilibrium assembly of man-made supramolecular materials. *Chem. Soc. Rev.* **46**, 5519–5535 (2017).
25. Das, K., Gabrielli, L. & Prins, L. J. Chemically fueled self-assembly in biology and chemistry. *Angew. Chem. Int. Ed.* **60**, 20120–20143 (2021).
26. Mattia, E. & Otto, S. Supramolecular systems chemistry. *Nat. Nanotechnol.* **10**, 111–119 (2015).
27. Sorrenti, A., Leira-Iglesias, J., Sato, A. & Hermans, T. M. Non-equilibrium steady states in supramolecular polymerization. *Nat. Commun.* **8**, 15899 (2017).
28. Geertsema, E. M., van der Molen, S. J., Martens, M. & Feringa, B. L. Optimizing rotary processes in synthetic molecular motors. *Proc. Natl Acad. Sci. USA* **106**, 16919–16924 (2009).
29. Wilcken, R., Gerwien, A., Huber, L. A., Dube, H. & Riedle, E. Quantitative in-situ NMR illumination for excitation and kinetic analysis of molecular motor intermediates. *ChemPhotoChem* **6**, e202100232 (2022).
30. Corra, S. et al. Artificial supramolecular pumps powered by light. *Chem. Eur. J.* **27**, 11076–11083 (2021).
31. Canton, M. et al. Second-generation light-fueled supramolecular pump. *J. Am. Chem. Soc.* **143**, 10890–10894 (2021).
32. Nitschke, P., Lokesh, N. & Gschwind, R. M. Combination of illumination and high resolution NMR spectroscopy: key features and practical aspects, photochemical applications, and new concepts. *Prog. Nucl. Magn. Reson. Spectrosc.* **114**, 86–134 (2019).
33. Baroncini, M., Silvi, S., Venturi, M. & Credi, A. Reversible photoswitching of rotaxane character and interplay of thermodynamic stability and kinetic lability in a self-assembling ring–axle molecular system. *Chem. Eur. J.* **16**, 11580–11587 (2010).
34. Blackmond, D. G. "If pigs could fly" chemistry: a tutorial on the principle of microscopic reversibility. *Angew. Chem. Int. Ed.* **48**, 2648–2654 (2009).
35. Ross, R. T. Some thermodynamics of photochemical systems. *J. Chem. Phys.* **45**, 1–7 (1966).
36. Porter, G. Transfer and storage of chemical and radiation potential. *J. Chem. Soc., Faraday Trans. 2* **79**, 473–482 (1983).
37. Penocchio, E., Rao, R. & Esposito, M. Nonequilibrium thermodynamics of light-induced reactions. *J. Chem. Phys.* **155**, 114101 (2021).
38. Onsager, L. Reciprocal relations in irreversible processes. I. *Phys. Rev.* **37**, 405–426 (1931).
39. Astumian, R. D. & Bier, M. Mechanochemical coupling of the motion of molecular motors to ATP hydrolysis. *Biophys. J.* **70**, 637–653 (1996).
40. Astumian, R. D. Stochastic conformational pumping: a mechanism for free-energy transduction by molecules. *Annu. Rev. Biophys.* **40**, 289–313 (2011).
41. Kondepudi, D. & Prigogine, I. *Modern Thermodynamics: From Heat Engines to Dissipative Structures* (Wiley, 1998).
42. Rao, R. & Esposito, M. Nonequilibrium thermodynamics of chemical reaction networks: wisdom from stochastic thermodynamics. *Phys. Rev. X* **6**, 041064 (2016).
43. Demirel, Y. & Gerbaud, V. in *Nonequilibrium Thermodynamics* 4th edn, Ch. 8 (Elsevier, 2019).
44. Lehn, J.-M. Perspectives in chemistry—aspects of adaptive chemistry and materials. *Angew. Chem. Int. Ed.* **54**, 3276–3289 (2015).
45. Ries, H. & McEvoy, A. J. Chemical potential and temperature of light. *J. Photochem. Photobiol. A* **59**, 11–18 (1991).
46. Penocchio, E., Rao, R. & Esposito, M. Thermodynamic efficiency of dissipative chemistry. *Nat. Commun.* **10**, 3865 (2019).
47. Amano, S. et al. Insights from an information thermodynamics analysis of a synthetic molecular motor. *Nat. Chem.* https://doi.org/10.1038/s41557-022-00899-z (2022).
48. Sabatino, A., Penocchio, E., Ragazzon, G., Credi, A. & Frezzato, D. Individual-molecule perspective analysis of chemical reaction networks: the case of a light-driven supramolecular pump. *Angew. Chem. Int. Ed.* **58**, 14341–14348 (2019).

Publisher's note Springer Nature remains neutral with regard to jurisdictional claims in published maps and institutional affiliations.

© The Author(s), under exclusive licence to Springer Nature Limited 2022

Methods

Dissipative operation of the supramolecular pump. Typically, an equimolar solution of **1** and *E*-**2**$^+$ in air-equilibrated CD_3CN (8.9×10^{-3} M, 0.6 ml) was allowed to reach thermodynamic equilibrium in the dark at 298 K. Subsequently, a non-equilibrium mixture of the corresponding free and complexed *Z*-**2**$^+$ was obtained by photoisomerization of the azobenzene unit. Photoisomerization was performed in situ using a light-emitting diode Illuminator (1.5 W; λ_{max} = 369 nm; full-width at half-maximum, 15.56 nm) equipped with a bandpass filter centred at 365 ± 5 nm. A quartz optical fibre (core 1,000 µm, 5 m) was used to channel light to the solution. The terminal end of the optical fibre (the quartz core) was exposed and submerged into the solution within the NMR tube. Upon reaching a stable *Z*/*E* composition (PSS), irradiation was interrupted (dark, relaxation to local equilibrium) or regulated (light on, dissipative operation) using the appropriate neutral density filter and the time-dependent concentration changes of the species were followed using ^{1}H NMR.

Dynamic simulations. The linear time-variant (LTV) system of differential equations describing the pumping cycle was implemented considering three subsequent time-invariant steps (LTI): (a) equilibration in the dark, (b) photoisomerization and (c) operation regime. For each LTI step the reaction rates for all processes and species concentrations were computed separately at any time point. The final concentrations were taken as initial conditions for the subsequent LTI step.

Data availability

All data needed to evaluate the conclusions are present in the main text and/or the Supplementary Information. Additional data related to this paper may be requested from the corresponding author on reasonable request. Source data are provided with this paper.

Acknowledgements

Financial support from the EU (H2020 ERC AdG 692981 and ERC-2015-CoG n. 681456) and the Ministero dell'Università e della Ricerca (PRIN 20173L7W8K and 201732PY3X, FARE R16S9XXKX3) is gratefully acknowledged.

Author contributions

S.C. and J.G. synthesized the compounds. M.T.B., S.C., S.S. and M.B. designed and performed the kinetic experiments and analysed the data. S.C. carried out numerical simulations. E.P. and M.E. performed the thermodynamic analysis. A.C. and S.C. wrote the manuscript with input from all authors. All authors discussed the results and commented on the manuscript. A.C. conceived the project and directed the research.

Competing interests

The authors declare no competing interests.

Additional information

Supplementary information The online version contains supplementary material available at https://doi.org/10.1038/s41565-022-01151-y.

Correspondence and requests for materials should be addressed to Alberto Credi.

Peer review information *Nature Nanotechnology* thanks the anonymous reviewers for their contribution to the peer review of this work.

Reprints and permissions information is available at www.nature.com/reprints.

nature portfolio

https://doi.org/10.1038/s41565-022-01151-y

Supplementary information

Kinetic and energetic insights into the dissipative non-equilibrium operation of an autonomous light-powered supramolecular pump

In the format provided by the authors and unedited

Kinetic and energetic insights into the dissipative non-equilibrium operation of an autonomous light-powered supramolecular pump

Stefano Corra,[‡,1,2] Marina Tranfić Bakić,[‡,1,2] Jessica Groppi,[1] Massimo Baroncini,[1,4] Serena Silvi,[1,3] Emanuele Penocchio[5], Massimiliano Esposito[5], Alberto Credi[1,2,*]

[1] CLAN-Center for Light Activated Nanostructures, Istituto ISOF-CNR, via Gobetti 101, 40129 Bologna, Italy

[2] Dipartimento di Chimica Industriale "Toso Montanari", Università di Bologna, viale del Risorgimento 4, 40136 Bologna, Italy

[3] Dipartimento di Chimica "G. Ciamician", Università di Bologna, via Selmi 2, 4126 Bologna, Italy

[4] Dipartimento di Scienze e Tecnologie Agro-alimentari, Università di Bologna, viale Fanin 44, 40127 Bologna, Italy

[5] Department of Physics and Materials Science, University of Luxembourg, L-1511 Luxembourg City, G. D. Luxembourg

[‡] these authors contributed equally to the work

SUPPLEMENTARY INFORMATION

1. Materials and methods 2
2. Synthesis and characterization of the supramolecular pump 3
3. Operation of the Supramolecular Pump 6
4. Fitting and Numerical Simulations 10
5. Thermodynamic Analysis 14
7. References 23

1. Materials and methods

General materials. All reagents and chemicals were purchased from Sigma-Aldrich or VWR international and used as received unless otherwise stated. Flash column chromatography was performed using Sigma Aldrich Silica 40 (230-400 mesh size or 40-63 μm) as the stationary phase. Thin layer chromatography was performed on TLC Silica gel 60 F254 coated aluminum plates from Merck.

NMR Spectroscopy. NMR spectra were recorded on an Agilent DD2 spectrometer operating at 500 MHz. Chemical shifts are quoted in parts per million (ppm) relative to tetramethylsilane using the residual solvent peak as a reference standard and all coupling constants (*J*) are expressed in Hertz (Hz).

NMR Photochemistry Photochemical reactions were performed in air-equilibrated CD_3CN solutions at 298 K inside NMR tubes in the spectrometer probehead, using a Prizmatix UHP-T-365-SR LED Illuminator (1.5 W, λ_{max}= 369 nm, FWHM, 15.56 nm) equipped with an FCA-SMA adaptor for optical fiber. The desired irradiation wavelength of 365 nm was selected using the appropriate hard coated OD 4.0 bandpass filter. Neutral density AR coated filters were used to regulate intensity of incident light when required. Quartz optical fiber (core 1000 μm, 5 m) equipped with a SMA connector on one end was purchased from Thorlabs. The other end of the optical fiber was scraped to remove the protective coatings, exposing the quartz core, and submerged into the solution within the NMR tube to be irradiated. The emission spectra of the light source (optical fiber end with protective coatings removed) were measured with an AVANTES Star Line AvaSpec-ULS2048CL-EVO-RS spectrometer. The emission intensity was selected using the appropriate neutral density filter with known optical density, purchased from Edmund Optics.

Least square fitting and numerical simulations. Fitting of the experimental data to the appropriate kinetic model was performed using Berkeley Madonna 10. Numerical simulations were performed with MATLAB R2018b implementing the kinetic model including all the kinetic and photokinetic equations as a system of differential equations that was solved numerically with ode15s solver.

2. Synthesis and characterization of the supramolecular pump

2.1 Synthesis of the axle

The axle was synthesized according to a previously published procedure.[1] Analytical data were in line with those previously reported.

2.2. ^{1}H NMR characterization of axles and complexes

^{1}H NMR spectra of *E* and *Z* axles and complexes were consistent with those previously reported in ref. 1 and summarized in Fig. S1.

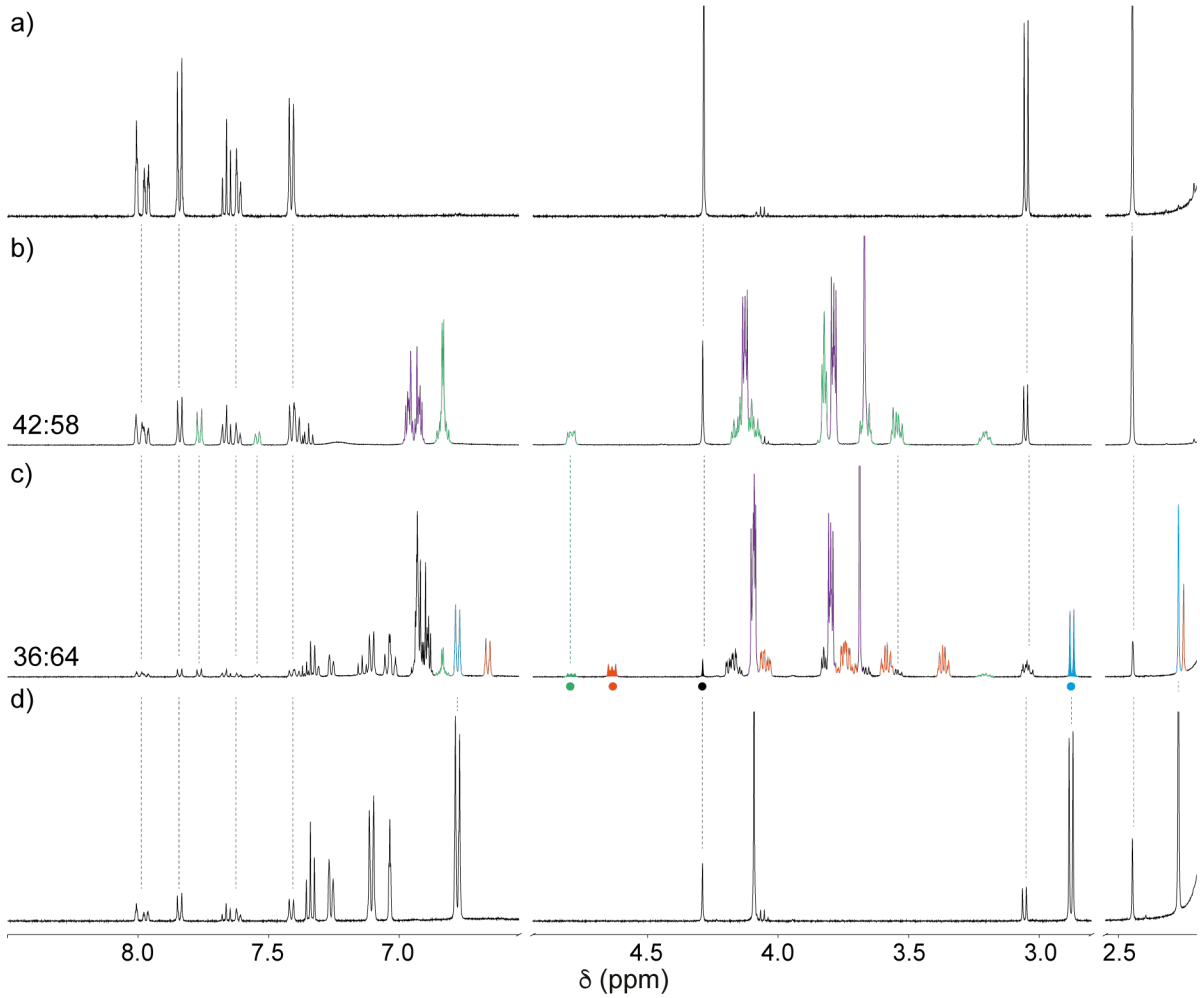

Figure S1. Typical ^{1}H NMR spectra (500 MHz, CD_3CN, 298 K) of a) *E*-**2**$^+$. b) A 1:1 equilibrated mixture of *E*-**2**$^+$ and **1**, the signals univocally associated with the complex are highlighted in green, the signals of free **1** are highlighted in purple. c) The same sample after exhaustive irradiation (λ_{irr} = 365 nm, 30 min) and equilibration for 3 hours in dark. Signals of free *Z*-**1**$^+$ are highlighted in cyan, signals univocally attributed to the *Z*-complex are highlighted in orange. d) same sample as (a) after exhaustive irradiation (λ_{irr} = 365 nm, 30 min). The dots underneath the filled signals in (c) mark the signals univocally assigned to the species followed for the kinetic measurements: green: **1**·*E*-**2**$^+$; orange: **1**·*Z*-**2**$^+$; cyan: *Z*-**2**$^+$; black: *E*-**2**$^+$. Ratios in (b) and (c) indicate the complex associated fraction (complex:axle) obtained by integration of univocally identified, non-overlapping, signals for complex and free axle.

2.3 NMR Photochemistry

About 6 cm of the coating were removed from the terminal end of a quartz optical fiber (~5 m). The exposed quartz core was sanded in order to diffuse light into solution. In a typical NMR experiment, the exposed core of the fiber was immersed in 0.6 mL of an equimolar solution (~9×10^{-3} M) of *E*-**2**$^{+}$ and **1** inside an NMR tube. The other extremity of the fiber was connected to a LED apparatus equipped with two filter holders. The wavelength of emission was 365 ± 5 nm, selected using a hard coated bandpass interference filter. The number of incident photons was selected using an additional neutral density (ND) filter with known optical density.

2.3.1 Optical Fiber Emission Spectra

The polychromatic emission spectra of the light source at different light intensities obtained with the appropriate neutral density filter consist of broad bands with a maximum at 369 nm (Fig. S2a). The 365 ± 5 nm interference filter significantly narrowed the emission spectrum (Fig. S2b). In both setups, the integral of the emission bands, which is proportional to the output power, changes linearly with the transmittance of the ND filter (insets in Fig. S2). The emission spectra reported in Fig. S2b correspond to the "monochromatic" irradiation wavelength used in all the photochemical experiments.

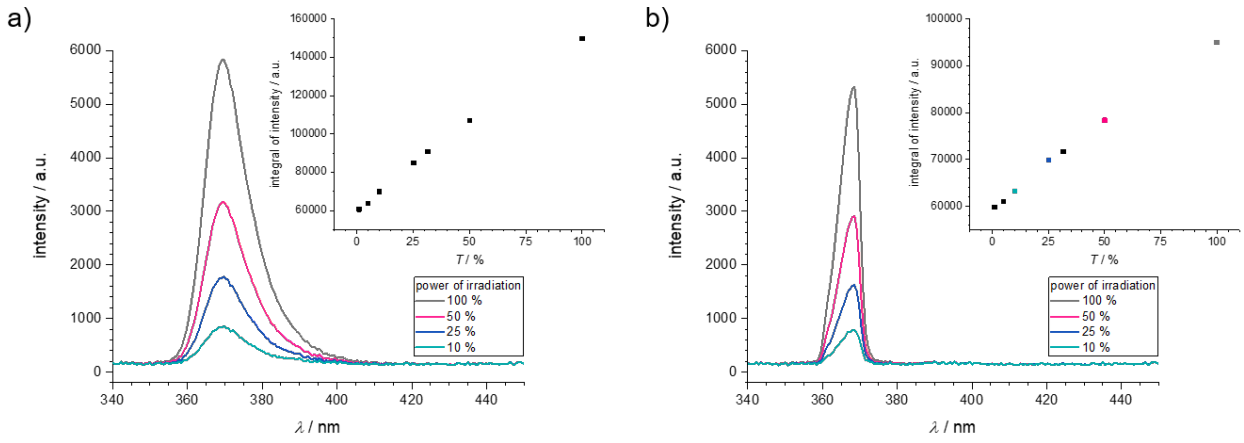

Figure S2. Emission spectra of the light source a) polychromatic setup b) monochromatic setup. In the inset the plot of integrated intensity on the percentage of transmitted light achieved with the appropriate ND filter. Light intensity values corresponding to those used for pump operation are reported in the same color as the corresponding spectrum in the inset.

2.3.2 NMR Chemical Actinometry

In order to estimate the photon flow of the optical fiber chemical actinometry was performed using the same experimental setup as for the molecular pump irradiation experiments using azobenzene as the actinometer. A solution of azobenzene in CD_3OD (1.19×10^{-2} M, 0.6 mL) was irradiated at 365 nm inside the NMR tube and *E*→*Z* isomerization was followed by ^{1}H NMR (Fig. S3). Photostationary state (PSS) was reached in about 50 min. The photon flow ($q_{n,p}$) and the ε_Z were

determined by least-square fitting of the concentration profiles of *E*- and *Z*-azobenzene to the photokinetic equation set (see below eq. S8 and S9), considering the thermal *Z*→*E* isomerization. Molar absorption coefficient for *E*-azobenzene[2] and quantum yields[3] in methanol were taken from literature data, while the obtained molar absorption coefficient for *Z*-azobenzene at 365 nm is in line with the reported data[3]. A photon flow ($q_{n,p,max}$) of 4.4×10^{-8} Einstein s^{-1} was obtained, corresponding to an output power of about 14 mW.

Table S1. Photophysical data of azobenzene in methanol used for actinometry.

ε (M^{-1} cm^{-1})		$\phi^{E\text{-}Z}$ [a]	$\phi^{Z\text{-}E}$ [a]	k_{Δ} (s^{-1})
***E*-azobenzene**	***Z*-azobenzene**			
375[b]	92[c]	0.12	0.34	1.0×10^{-6}

[a]Ref. 3. [b]Ref. 2. [c]Fitted parameter.

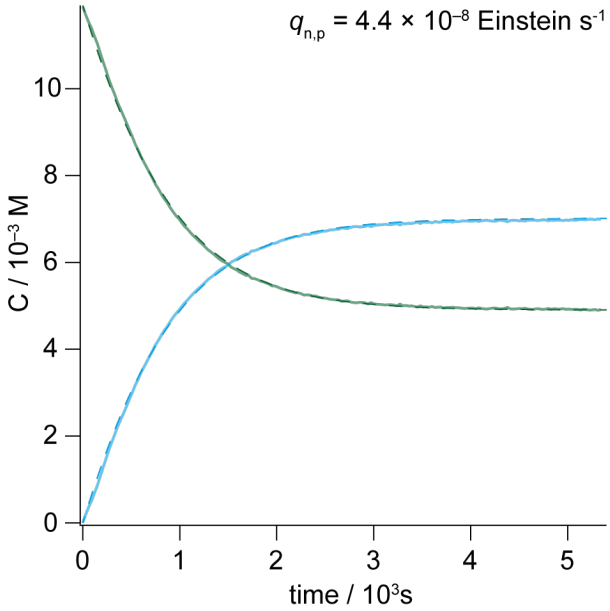

Figure S3. ^{1}H NMR kinetic of photoconversion of azobenzene (1.19×10^{-2} M, CD_3OD, 298 K). *E*-azobenzene: green line, *Z*-azobenzene: blue line. Solid lines represent the experimental concentration profile, dashed lines are least square fitting to the photokinetic equations set.

Since the radiant power increases linearly with the transmittance (Fig. S2), the number of incident photons for the numerical simulations (see below) was calculated from the 100% intensity diminished by the optical density of the filter used according to the following equation.

$$q_{n,p} = q_{n,p,max} \times 10^{-O.D.} \quad \text{(S1)}$$

3. Operation of the Supramolecular Pump

Typically, an equimolar mixture of **1** and *E*-**2**$^+$ (~9 × 10^{-3} M) was allowed to reach thermodynamic equilibrium in the dark, then a non-equilibrium mixture of *Z* axle and *Z* complex was obtained by photoisomerization of the azobenzene unit. Photoisomerization was performed *in situ* using the setup described in section 2.3.

Upon reaching a stable *Z*/*E* composition (PSS) irradiation was interrupted (Fig. S4, black trace) or reduced (Fig. S4, colored traces) and the time-dependent changes in concentration of the photoactive species were followed by ^{1}H NMR.

The initial concentrations of **1** and *E*-**2**$^+$ used in each experiment are reported in Table S2.

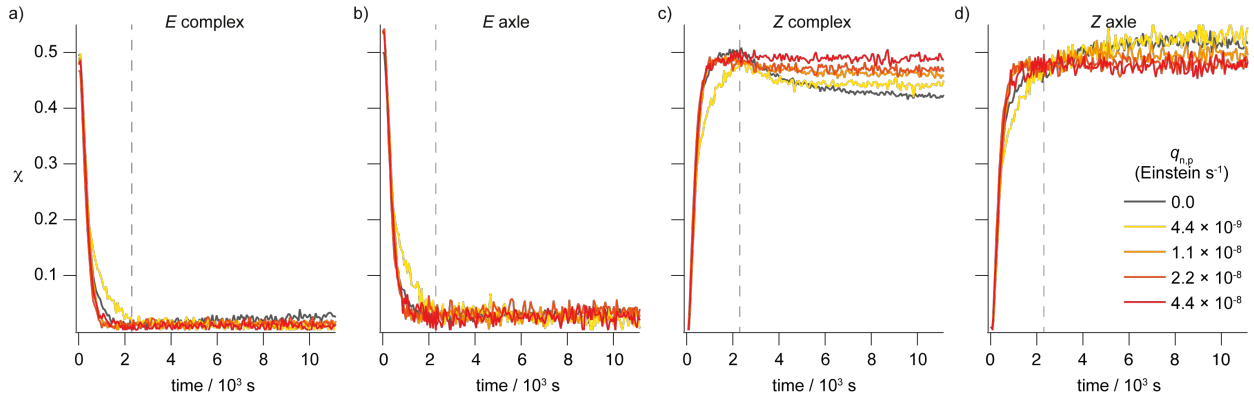

Figure S4. Time-dependent molar fraction profiles of *E* complex (a), *E* axle (b), *Z* complex (c), and *Z* axle (d) at different light intensities generated by light-induced isomerization of an equilibrated mixture of *E*-**2**$^+$ and **1**. The gray dashed line indicates the time at which PSS is reached. Data obtained from ^{1}H NMR data (500 MHz, CD_3CN, 298 K, initial concentrations for each experiment are reported in Table S2).

Table S2. Experimental initial concentrations of **1** and *E*-**2**$^+$.

$q_{n,p}$ (Einstein s^{-1})	0	4.4×10^{-9}	1.1×10^{-8}	2.2×10^{-8}	4.4×10^{-8}
(% of $q_{n,p,max}$)	0%	10%	25%	50%	100%
$[2^+]_0$ (M)	8.91×10^{-3}	7.43×10^{-3}	7.43×10^{-3}	7.43×10^{-3}	8.17×10^{-3}
$[1]_0$ (M)	8.98×10^{-3}	7.48×10^{-3}	7.48×10^{-3}	7.48×10^{-3}	8.23×10^{-3}

The complete closed reaction network describing the pumping cycle for compounds **1** and **2**$^+$ is reported in Scheme S1. This set of six reactions (four thermal and two photochemical) was implemented in appropriate kinetic models for fitting or simulating the experimental data (see section 4).

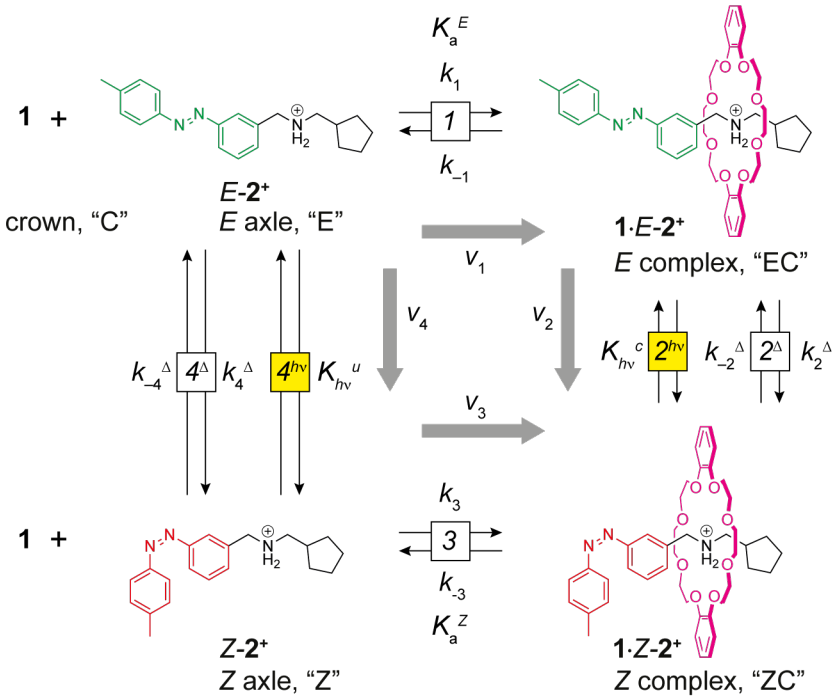

Scheme S1. Complete reaction network for compound **2**$^+$ and **1** used to fit and simulate the experimental behavior. Reactions are numbered clockwise starting from the top. "*K*" and "*k*" indicate equilibrium and rate constants respectively. "*h*ν" and "Δ" indicate the photochemical and thermal (*E*→*Z* and *Z*→*E*) isomerization processes respectively. Conventionally, the rates of reaction are positive for the reaction read from left to right and from top to bottom (gray arrows).

3.1 Cycling Rate

Under light irradiation, at the steady state the rates of all reactions must be equal in magnitude and their value corresponds to the cycling rate. The rate of reaction 3 was determined using the appropriate rate law (equation 1 of the manuscript) and the experimental concentration of complex, axle, and macrocycle. The steady state rates reported in the manuscript were measured by averaging the rate values over the last 15 minutes.

3.2 Cycle Quantum Yield

The cycle quantum yield (Φ_{cy}) represents the number of cycles performed in a given interval of time divided by the corresponding number of photons absorbed in the same time interval (equation S2). The number of moles of photons absorbed by the system per unit time was determined from the photons emitted by the light source considering the absorbance of the solution at 365 nm (section 2.2). The number of moles of pumps that completed a cycle in a given time is equal to the rate of cycling multiplied by the time interval and by the volume of the irradiated solution. The rate of cycling at steady state was measured from the rate of reaction 3 (section 3.1).

$$\Phi_{cy} = \frac{N_{cycles}}{N_{ph,abs}} = \frac{v_{cycling} \times \Delta t \times V}{q_{n,p}\left(1-10^{-A}\right) \times \Delta t} \tag{S2}$$

3.3 Kinetic Asymmetry

With reference to Scheme S1, the kinetic asymmetry (ratcheting constant, K_r) of the cycle can be rigorously quantified as:[4]

$$K_r = \frac{r_1 r_2 r_{-3} r_{-4}}{r_{-1} r_{-2} r_3 r_4} \tag{S3}$$

where, r_i and r_{-i} are the rates of the *i*-th process forward and backward respectively. Since the reactions describe a closed cycle and considering that the rate for processes 2 and 4 is the sum of the photochemical and thermal reaction rates ($r_i = r_i^{h\nu} + r_i^{\Delta}$), K_r can also be written in terms of the rate constants of the processes reported in Scheme S1:

$$K_r = \frac{k_1\left(k_2^{h\nu} + k_2^{\Delta}\right)k_{-3}\left(k_{-4}^{h\nu} + k_{-4}^{\Delta}\right)}{k_{-1}\left(k_{-2}^{h\nu} + k_{-2}^{\Delta}\right)k_3\left(k_4^{h\nu} + k_4^{\Delta}\right)} = K_a^E \frac{F_{h\nu}\varepsilon_{EC}\phi_{EC} + k_2^{\Delta}}{F_{h\nu}\varepsilon_{ZC}\phi_{ZC} + k_{-2}^{\Delta}} (K_a^Z)^{-1} \frac{F_{h\nu}\varepsilon_Z\phi_Z + k_{-4}^{\Delta}}{F_{h\nu}\varepsilon_E\phi_E + k_4^{\Delta}}$$

Where $F_{h\nu} = \frac{q_{n,p} \cdot b}{V} \frac{\left(1-10^{-A}\right)}{A}$ and $A = b \cdot \sum_i \varepsilon_i \cdot [i]$.

In the dark ($q_{n,p}$ = 0) $F_{h\nu}$ is null and K_r = 1 due to the microscopic reversibility of the thermal processes.[5] Conversely, in case of irradiation ($q_{n,p}$ > 0), the kinetic constants for thermal isomerization reactions (indicated with a "Δ" superscript) can be neglected with respect to the photochemical ones. As a result, the light-dependent parts of the equation simplify to the photostationary state composition for axle and complex. Moreover, for the present system is fair to assume that these are equally populated ($K_{h\nu}^{u} = K_{h\nu}^{c}$) and therefore:

$$K_r \approx K_a^E \frac{\varepsilon_{EC}\phi_{EC}}{\varepsilon_{ZC}\phi_{ZC}} (K_a^Z)^{-1} \frac{\varepsilon_Z\phi_Z}{\varepsilon_E\phi_E} = K_a^E K_{h\nu}^c (K_a^Z)^{-1} (K_{h\nu}^u)^{-1} \approx \frac{K_a^E}{K_a^Z} = 2$$

In Table S3 are reported the absolute rates of reaction for all processes obtained from numerical simulations (see section 4.2) and the ratcheting constants at different photon flows calculated using equation S3.

Table S3. Computed forward and backward reaction rates obtained from numerical simulations and calculated ratcheting constants.

	$q_{n,p}$ (Einstein s^{-1})	4.4×10^{-9}	1.1×10^{-8}	2.2×10^{-8}	4.4×10^{-8}
thermal reactions	**r_1 (10^{-6} M s^{-1})**	5.70	5.34	5.33	5.90
	r_{-1} (10^{-6} M s^{-1})	5.65	5.24	5.16	5.59
	r_3 (10^{-6} M s^{-1})	0.625	0.575	0.526	0.599
	r_{-3} (10^{-6} M s^{-1})	0.676	0.679	0.692	0.906
photoreactions	**r_2 (10^{-6} M s^{-1})**	0.213	0.497	0.979	2.09
	r_{-2} (10^{-6} M s^{-1})	0.147	0.378	0.797	1.77
	r_4 (10^{-6} M s^{-1})	0.192	0.470	0.952	1.99
	r_{-4} (10^{-6} M s^{-1})	0.234	0.566	1.11	2.29
	K_r[a]	1.9	1.9	2.0	2.2

[a]Calculated using equation S3 from computed reaction rates.

4. Fitting and Numerical Simulations

4.1 Fitting of the dethreading kinetic

Second order threading rate constant ($k_{in}^{E} = k_1$) and equilibrium constant (K_a^{E}) for the *E* isomer were determined independently by UV-Vis and ^{1}H NMR.[1] The rate constant of dethreading of compound *Z*-**2**$^+$ (k_{-3}) was determined by fitting of the time-dependent concentration profiles of *Z* axle and *Z* complex reaching the local according to a kinetic model including the thermal reactions of Scheme S1. The average value obtained from four independent "relaxation" experiments (black trace in figure S4) is (2.3±0.4)×10^{-4} s^{-1}, which is in excellent agreement with the previously reported data (Table S4) and was used in all the following calculations.

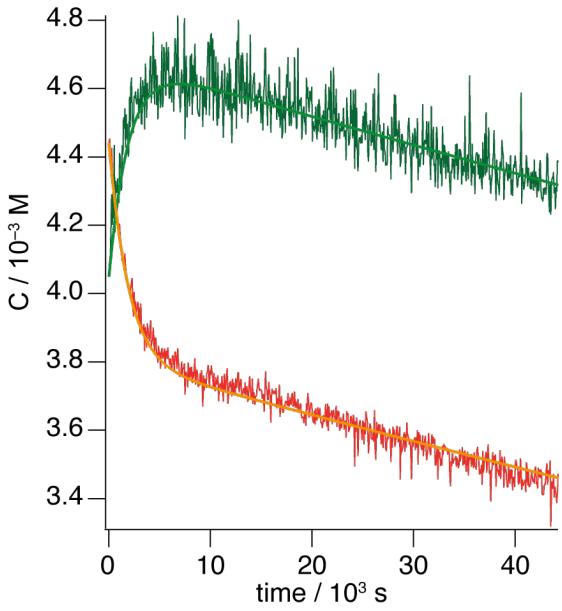

Figure S5. Typical kinetic of equilibration of a mixture of *Z*-**2**$^+$ and **1**, generated by fast light-induced isomerization of the corresponding equilibrated mixture of *E*-**2**$^+$ and **1**. Data obtained from ^{1}H NMR measurements (500 MHz, CD_3CN, 298 K). *Z* complex: red trace; *Z* axle: green trace. Solid lines represent the least square fitting according to the thermal reactions of scheme S1. Conditions: CD_3CN, *C* = 8.9 mM, 298 K.

Table S4. Comprehensive table of the experimental thermodynamic, kinetic, photophysical, and photochemical parameters for axle *E*-**2**$^+$, *Z*-**2**$^+$, and for the corresponding [2]pseudorotaxane in air-equilibrated CH_3CN.[a]

	K_a (M^{-1})	k_{in} (M^{-1} s^{-1})	k_{out} (s^{-1})	k_{Δ} (s^{-1})	ϕ[b]	ε_{365} (M^{-1} cm^{-1})
E-**2**$^+$	[c]	[c]	[c]	[c]	0.23 ($E\rightarrow Z$)	3900
Z-**2**$^+$	[c]	[c]	[c]	1.9×10^{-6}	0.58 ($Z\rightarrow E$)	< 100
1·*E*-**2**$^+$	230 ± 30	16[d]	0.07[e]	[c]	0.22 ($E\rightarrow Z$)	4800
1·*Z*-**2**$^+$	170 ± 30 115 ± 35[f]	$3.1\pm0.8\times10^{-2}$ [g]	$2.7\pm0.5\times10^{-4}$ [g] *$2.3\pm0.4\times10^{-4}$* [h]	4.8×10^{-6}	0.59 ($Z\rightarrow E$)	< 100

[a]Data reported in ref. 1. *Italicized* values were newly determined in this work. [b]Determined at 365 nm. The corresponding isomerization process is given in brackets. [c]Parameter is not relevant for the compound. [d]Determined by stopped-flow UV-Vis absorption method. [e]Calculated as k_{in}/K_a. [f]Calculated as k_{in}/k_{out}. [g]Determined by non-linear regression of the time-dependent ^{1}H NMR concentration profiles. [h]Same as (g) but determined in *this work* by regression of the dethreading kinetic. This value was used as the basis for the k_{-3} in the numerical simulations (see table S4).

4.2 Numerical Simulations

The kinetic behavior of the reaction network was simulated taking into consideration all the thermal and photochemical reactions in scheme S1. The reaction rates for all processes were computed separately at any point in time solving the linear system of differential equations (S4 to S8) that defines the pumping cycle with a stiff ODE solver (ode15s).

Concerning the implementation, the linear system describing the pumping cycle is time-variant (LTV), therefore simulations were carried out considering three time-invariant steps (LTI): a) equilibration, b) photoisomerization, and c) operation regime. The solutions from the previous LTI were taken as initial conditions for the subsequent one. The system is assumed to be in well-mixed conditions. Thus, diffusion of species is never considered rate limiting and all concentrations used in the rate laws are homogeneous in space. Details for the three steps are given below:

a) First the macrocycle and *E*-axle association in the dark was simulated using the initial experimental concentrations of *E*-**2**$^+$ and **1** as initial conditions for the numerical solution. A photon flow of 0.0 Einstein s^{-1} ("light off") was set in this step (photochemical rates are neglected). A close match between the simulated and experimental equilibrium composition in the dark was obtained.

b) Starting from these equilibrium concentrations of *E* axle and *E* complex the isomerization was simulated using the photokinetic equations (eq. S8). In this step the photon flow was set to the value of 4.4×10^{-8} Einstein s^{-1} for about 35 min, consistently with the experimental

procedure. Pleasingly, the simulated PSS concentrations (>95% conversion to *Z* isomers) matched very closely the experimental ones (Fig. S6) validating this methodology of simulation and the actinometry results (section 2.3).

c) Finally, from the simulated PSS concentrations the photon flow was set to the actual experimental value, and the system was allowed to reach the local equilibrium state or the kinetic steady state respectively in absence or presence of the light. Five possible photon flows ranging from 0.0 to 4.4×10^{-8} Einstein s^{-1} were used in the simulations in line with the experiments.

The rates of thermal reactions (*1*,*3*, 2^{Δ}, and 4^{Δ}) were computed with the corresponding rate equations (S4 to S7). The rate constants of reaction 3 were adjusted within the experimental error to achieve the best overlay with the experimental concentration profiles (table S4). The rate constants for the thermal *E*→*Z* isomerization reactions (k_2^{Δ} and k_4^{Δ}), included in Scheme 1 for completeness, were neglected in the simulations. As a result, reactions 2^{Δ} and 4^{Δ} appear as unidirectional processes that convert *Z* isomers to the corresponding *E* form (equations S6 and S7).

Reaction 1: $$v_1 = k_1[E\ axle][\mathbf{1}] - k_{-1}[E\ complex] \quad \text{(S4)}$$

Reaction 3: $$v_3 = k_3[Z\ axle][\mathbf{1}] - k_{-3}[Z\ complex] \quad \text{(S5)}$$

Reaction 2^{Δ}: $$v_{2\Delta} = k_2^{\Delta}[Z\ complex] \quad \text{(S6)}$$

Reaction 4^{Δ}: $$v_{4\Delta} = k_4^{\Delta}[Z\ axle] \quad \text{(S7)}$$

Where the Δ superscripts refer to the thermal *Z*→*E* isomerization process.

Rates of *E*→*Z* and *Z*→*E* photochemical isomerization for the free and complexed axles (reactions $2^{h\nu}$ and $4^{h\nu}$) were calculated using the photokinetic rate law (S8). Experimental quantum yields (ϕ) and molar absorption coefficients (ε) determined at 365 nm, as well as the photon flow determined by chemical actinometry ($q_{n,p,\mathrm{max}}$) were used. The absorbance of the mixture at the irradiation wavelength (A_{TOT}) was calculated according to Beer-Lambert's law at any point in time from the calculated mixture composition. Equation S8 is the general photokinetics equation[6] for the photoisomerization of the *i*-th species (*i* = *E* axle, *Z* axle, E complex, *Z* complex).

$$v_i = \frac{q_{n.p}\cdot b}{V}\cdot \phi^i \ \cdot \varepsilon_i \cdot [i]\frac{1-10^{-A_{TOT}}}{A_{TOT}} \quad \text{(S8)}$$

It must be noted that each photoactive species needs two photokinetic rate laws accounting for both *E*→*Z* and *Z*→*E* photochemical isomerization processes.

A total of four photokinetic equations plus the six rate laws are needed to appropriately simulate the pumping cycle (Scheme S1). In Fig. S6 (top row) the simulated concentration profiles of all the

photoactive species are displayed. In table S5 the parameters used in the dynamic simulations reported in Fig. 3 of the main text and Fig. S6 are reported.

Table S5. Experimental initial concentrations of **1** and *E*-**2**$^+$, rate constants, and photophysical parameters used for the numerical simulations at the different photon flows.[a]

$q_{n,p}$ (Einstein s^{-1})	0	4.4×10^{-9}	1.1×10^{-8}	2.2×10^{-8}	4.4×10^{-8}
(% of $q_{n,p,max}$)	0%	10%	25%	50%	100%
$[2^+]_0$ (M)[b]	8.91×10^{-3}	7.43×10^{-3}	7.43×10^{-3}	7.43×10^{-3}	8.17×10^{-3}
$[1]_0$ (M)[b]	8.98×10^{-3}	7.48×10^{-3}	7.48×10^{-3}	7.48×10^{-3}	8.23×10^{-3}
k_3 (M^{-1} s^{-1})[c]	3.65×10^{-2}	3.7×10^{-2}	3.7×10^{-2}	3.5×10^{-2}	3.65×10^{-2}
k_{-3} (s^{-1})[d]	2.25×10^{-4}	2.1×10^{-4}	2.0×10^{-4}	2.0×10^{-4}	2.25×10^{-4}
ε_{EC}	4800	4800	4800	4800	4800
ε_{E}	3900	3900	3900	3900	3900
ε_{ZC}[e]	30	31	30	31	30
ε_{Z}[e]	40	40	40	40	40
$\phi^{E\rightarrow Z}$	0.23	0.23	0.23	0.23	0.23
$\phi^{Z\rightarrow E}$	0.58	0.58	0.58	0.58	0.58
$\phi^{EC\rightarrow ZC}$	0.22	0.22	0.22	0.22	0.22
$\phi^{ZC\rightarrow EC}$	0.59	0.59	0.59	0.59	0.59

[a]The parameters shaded in orange were adapted within the confidence interval of the experimental value to achieve a better overlay with the data. [b]Experimental concentration. [c]Adapted in the interval $(3.1\pm0.8)\times10^{-4}$ M^{-1} s^{-1}. [d]Adapted in the interval $(2.3\pm0.4)\times10^{-4}$ s^{-1}. [e]Value calculated in order for the ratio $\frac{\phi^{EZ}\varepsilon_E}{\phi^{ZE}\varepsilon_Z}$ to match the experimental composition at the PSS; minor modifications were performed to achieve a better overlay with the experimental data.

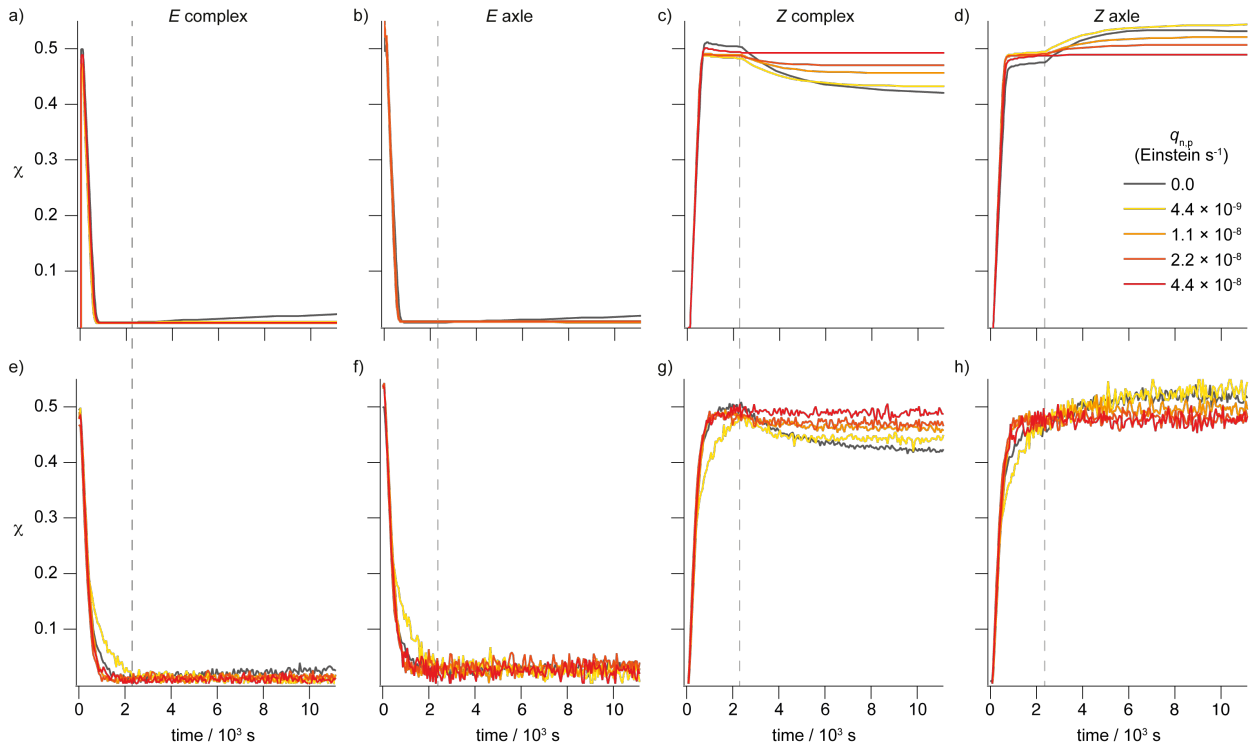

Figure S6. Simulated molar fraction profiles (top row) at different light intensities of all species generated by light-induced isomerization of an equilibrated mixture of *E*-**2**$^+$ and **1**. On the bottom row the corresponding experimental profiles (Fig. S4) are reported for comparison. *E* complex (a, e), *E* axle (b, f), *Z* complex (c, g), and *Z* axle (d, h). The gray dashed line indicates the time at which PSS is reached. Data obtained from ^{1}H NMR data (500 MHz, CD_3CN, 298 K, initial concentrations for each experiment are reported in Table S4).

5. Thermodynamic Analysis

All the following thermodynamic considerations are made in the steady state regime, unless otherwise specified, that is, analogously to equilibrium condition, time-invariant. The steady state concentrations of all species extracted from time-dependent ^{1}H NMR experiments are reported in table S6.

Table S6. Experimental and simulated molar concentrations of **1**, *E*-**2**$^+$, *Z*-**2**$^+$ and of the corresponding complexes at the local equilibrium (dark) or dissipative steady states (light on).

	$q_{n,p}$ (Einstein s^{-1})				
	Dark	**4.4×10^{-9}**	**1.1×10^{-8}**	**2.2×10^{-8}**	**4.4×10^{-8}**
[EC] (M)[a]	2.24×10^{-4}	8.07×10^{-5}	7.48×10^{-5}	7.34×10^{-5}	7.99×10^{-5}
[E] (M)[a]	2.00×10^{-4}	8.53×10^{-5}	8.32×10^{-5}	8.46×10^{-5}	9.01×10^{-5}
[ZC] (M)[b]	3.76×10^{-3}	3.28×10^{-3}	3.42×10^{-3}	3.49×10^{-3}	4.00×10^{-3}
[Z] (M)[b]	4.59×10^{-3}	3.96×10^{-3}	3.69×10^{-3}	3.57×10^{-3}	3.91×10^{-3}
[C] (M)[c]	4.95×10^{-3}	4.13×10^{-3}	3.94×10^{-3}	3.86×10^{-3}	4.13×10^{-3}

[a]Determined from dynamics simulation. [b]Experimental molar concentrations calculated from the mole fractions (observable) averaged over the last 15 min and the initial concentration of axle. [c]Determined applying mass balance considerations.

5.1 Chemical Potential of Reaction

The non-standard chemical potential of reaction (also known as thermodynamic affinity when taken with a minus sign) was calculated from the concentrations maintained at the kinetic steady state away from equilibrium according to equation S9.[7] At any point along the reaction coordinate the $\Delta\mu$ is given by the sum of the chemical potential of each species (μ_i) multiplied by the corresponding stoichiometric coefficient (negative for reagents). In particular, a positive value of $\Delta\mu$ corresponds to a steady state shifted towards the products ($\mu_P > \mu_R$), while the opposite holds for a negative $\Delta\mu$. For a generic reaction of the kind A + B $\rightarrow$ P the overall variation in chemical potential thus reads:

$$\Delta\mu = -\mu_A - \mu_B + \mu_P$$

Then:

$$\Delta\mu = -\mu_A^0 - RT\ln[A] - \mu_B^0 - RT\ln[B] + \mu_P^0 + RT\ln[P] = \underbrace{-\mu_A^0 - \mu_B^0 + \mu_P^0}_{\Delta\mu^0} + RT\ln\frac{[P]}{\underbrace{[A][B]}_{Q}}$$

$$\Delta\mu = RT\ln Q - RT\ln K \qquad \text{(S9)}$$

where K is the equilibrium constant of the reaction, Q is the reaction quotient. The sum of the non-standard chemical potential (thermodynamic affinities when taken with the opposite sign) along the cycle of scheme S1 is the free energy dissipated along one cycle of operation.

5.2 Thermodynamic of Radiation

Fig. S7a and b present a scheme of the irradiation setup used in this study, which served as the basis for the thermodynamic analysis. The first step of our thermodynamic analysis is to determine the concentration of photons in a volume element $dV_{cyl}(r)$ consisting of an infinitesimally thin cylindrical shell of thickness *dr* (inner radius *r* and outer radius *r* + d*r*) axial to the optical fiber and the NMR tube (highlighted in red Fig. S7c). The volume of the cylindrical shell is $dV_{cyl}(r) = \pi h((r+dr)^2 - r^2) = 2\pi h r dr$.

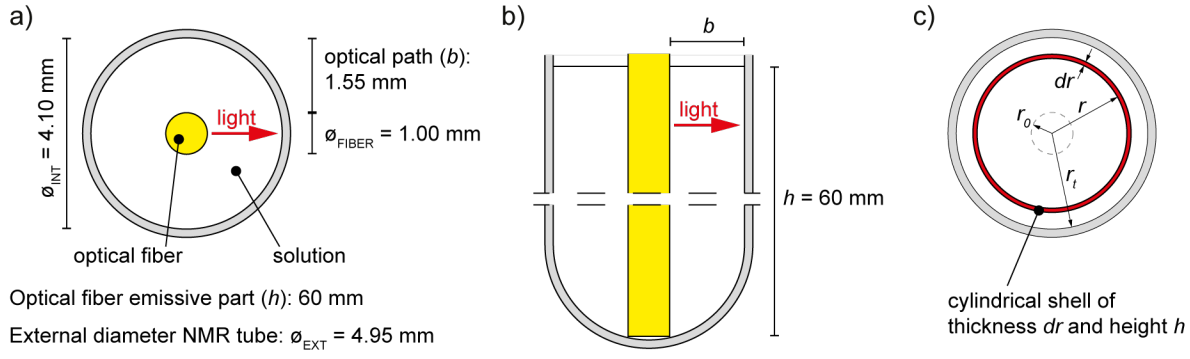

Figure S7. Scheme of the optical geometry and dimensions of the irradiation setup. a) Top view. b) Side view. c) Modelling of the infinitesimal volume travelled by light in a unit time used in the thermodynamic analysis (r_0 = 0.5 mm, r_t = ø$_{INT}$/2 = 2.05 mm).

The moles of photons in this volume ($dN_{h\nu}(r)$) can be computed by multiplying the number of moles of photons impinging on the inner surface per unit time ($q_{n,p}(r)$) by the time that light takes to travel the distance *dr* ($t = dr/c$, where "*c*" is the speed of light):

$$dN_{h\nu}(r) = q_{n,p}(r) \cdot t = \frac{q_{n,p}(r)}{c} dr$$

The molar concentration of photons in the volume $dV_{cyl}(r)$ is then:

$$n_{h\nu}(r) = \frac{dN_{h\nu}(r)}{dV_{cyl}(r)} = \frac{q_{n,p}(r)}{2\pi hcr} = \frac{q_{n,p}}{2\pi hc} \cdot \frac{10^{-(r-r_0)\sum_i \varepsilon_i[i]}}{r}$$

where the dependence of $q_{n,p}(r)$ on *r* has been expressed in terms of the Beer-Lambert's law and the total amount of photons emitted by the optical fiber ($q_{n,p}(r_0) \equiv q_{n,p}$). It is worth noting that the molar concentration of photons in the volume $dV_{cyl}(r)$ has, in principle, also a contribution n_{bb}^T (constant along *r*) from the black body emission of the solution due to its temperature *T*. However, such a contribution is negligible at any *r* when compared to that of the source at the wavelength and intensity considered.

To proceed with our analysis, we now define the effective temperature $T_{h\nu}(r)$ associated with the radiation in the volume $dV_{cyl}(r)$. Such a temperature is the one that a black body needs to have in order to generate a molar concentration of photons equal to $n_{h\nu}(r)$ in the interval selected by the interference filter (365±5 nm), and can be computed by solving numerically the following equation:

$$n_{h\nu}(r) = \int_{360\ nm}^{370\ nm} n_{bb}(\lambda) d\lambda = \int_{360\ nm}^{370\ nm} \frac{8\pi}{N_A \lambda^4} \cdot \frac{1}{e^{hc/\lambda k_B T_{h\nu}} - 1} d\lambda$$

where N_A is the Avogadro's number, *h* the Planck's constant, and k_B the Boltzmann's constant. The above equation uniquely defines $T_{h\nu}(r)$ and is well justified within the monochromatic assumption. Indeed, as all the photons impinging on the system are considered at the same frequency, the exact shape of their distribution in frequency in the interval selected by the interference filter has no role in the treatment, and can therefore be assumed to be the black body one ($n_{bb}(\lambda)$) without altering the final results. This has the major advantage that the radiation in the volume $dV_{cyl}(r)$ can be considered as a heat source at temperature $T_{h\nu}(r)$. Since the solvent acts as another heat source at temperature *T*, we can properly think of the molecular motor as a

thermal engine working by virtue of the temperature gradient between the radiation and the solvent. As a consequence, we can immediately conclude that the maximum efficiency at which the motor can convert the energy absorbed from the radiation into work in the volume $dV_{cyl}(r)$ is limited by Carnot's theorem:

$$\eta_C(r) = 1 - \frac{T}{T_{h\nu}(r)}$$

We can have a first idea of the thermodynamics of the motor by computing the average temperature of the radiation and the average Carnot's efficiency (Table S7).

$$\langle T_{h\nu} \rangle = \frac{1}{b}\int_{r_0}^{r_t} T_{h\nu}(r)dr$$

$$\langle \eta_C \rangle = \frac{1}{b}\int_{r_0}^{r_t} \eta_C(r)dr$$

Note that, by virtue of the inequality holding between the harmonic mean and the arithmetic mean of a positive defined function, we have that:

$$\langle \eta_C \rangle = 1 - T\,\langle \frac{1}{T_{h\nu}} \rangle \leq 1 - \frac{T}{\langle T_{h\nu} \rangle}$$

and therefore the Carnot's efficiency computed by using the average temperature of the hot heat source ($\langle T_{h\nu} \rangle$) provides an upper bound to the maximum efficiency of the whole system considered as a thermal engine.

To have further quantitative insights on the thermodynamic characterization of the system, we introduce the chemical potential of the radiation as:[8]

$$\mu_{h\nu}(r) = N_A h\nu \cdot \eta_C(r)$$

In this context, the chemical potential of the radiation can be interpreted as the part of the molar energy coming from the light source which is actually available to the system in the volume $dV_{cyl}(r)$ (the free energy in the volume). It is also the amount of energy which can be used to take the system away from thermodynamic equilibrium by performing work on it. From the above expression, whenever the concentration of photons in the volume $dV_{cyl}(r)$ is such that $T_{h\nu}(r) = T$, with a molar concentration of photons equal to n_{bb}^{T}, corresponding to the black body emission of the solution at the temperature *T*, the chemical potential of the radiation is null. Therefore, the radiation cannot perform any work on the system in that volume element. In this condition which

corresponds to the absence of radiation from the source the only possible steady state for the system is the equilibrium one. In Table S7, the average chemical potential for the five experimental regimes is reported. The average chemical potential of the radiation in the system is way larger than the thermal energy (*RT*) and about one order of magnitude higher than the free energy released upon hydrolysis of ATP to ADP in physiological conditions. Moreover, by increasing the light intensity, the average chemical potential of the radiation also increases, consistently with the system being brought farther away from equilibrium at higher photon fluxes.

Table S7. Average temperature of radiation ($\langle T_{h\nu} \rangle$), Carnot's efficiency ($\langle \eta_C \rangle$), and chemical potential of radiation ($\langle \mu_{h\nu} \rangle$) at the investigated photon flows.[a]

$q_{n,p}$ (Einstein s^{-1})	$\langle T_{h\nu} \rangle$ (K)	$\langle \eta_C \rangle$	$\langle \mu_{h\nu} \rangle$ (kJ mol^{-1})[a]
0	298	0	0[b]
4.4×10^{-9}	1917	0.844	277
1.1×10^{-8}	2007	0.851	279
2.2×10^{-8}	2081	0.857	281
4.4×10^{-8}	2159	0.862	282

[a]The energy of one mole of 365 nm photons was estimated as $N_A h\nu$ = 328 kJ mol^{-1}. [b]The actual value of photon flow at which the force is null is not 0 Einstein s^{-1}, but rather a very small value of photon flow corresponding to a black body at 298 K emitting around 365 nm.

5.3 Energy Dissipation and Storage

We now couple the thermodynamic description with the system's kinetics. The number of moles of photons absorbed by the system per unit of time in the volume element $dV_{cyl}(r)$ is:

$$dq_{n,p}(r) = q_{n,p}(r) - q_{n,p}(r+dr) = q_{n,p}(r)\left(1 - 10^{-dr\sum_i \varepsilon_i[i]}\right)$$
$$= q_{n,p}(r)\sum_i \varepsilon_i[i]dr + \mathcal{O}(dr^2)$$
$$\approx q_{n,p}(r)\sum_i \varepsilon_i[i]dr$$

from which we can compute the free energy absorbed by the system per unit of time ($\dot{W}$) in the same volume element as:

$$d\dot{W}(r) = \mu_{h\nu}(r)dq_{n,p}(r) = \mu_{h\nu}(r)q_{n,p}(r)\sum_i \varepsilon_i[i]dr$$

However, since the quantum yield of photoisomerization is not unitary for the considered processes, the actual amount of absorbed free energy which can perform work on the system, thus modifying the species concentrations, is:

$$d\dot{W}_{h\nu}(r) = \mu_{h\nu}(r) q_{n,p}(r) \sum_i \phi_i \varepsilon_i [i] dr$$

Were the quantum yields (ϕ_i) are included to account for the amount of absorbed free energy which is unavoidably dissipated without leading to photoisomerization.
The integral of $d\dot{W}_{h\nu}(r)$ over the space occupied by the solution and divided by the volume yields the input power of the molecular motor which appears in equation (2) of the main text, that is the work performed on the system by the radiation:

$$\dot{W}_{h\nu} = \frac{1}{V} \sum_i \phi_i \varepsilon_i [i]\, q_{n,p} \int_{r_0}^{r_t} \mu_{h\nu}(r)\, 10^{-(r-r_0)\sum_i \varepsilon_i [i]} dr$$

At any time, the free energy absorbed per unit time and volume can either be dissipated or stored in the system as free energy. This is expressed by equation (2) of the main text:

$$\dot{W}_{h\nu} = d_t G + T\dot{\Sigma}$$

where the dissipation rate per unit of volume is always positive ($T\dot{\Sigma} \geq 0$) according to the second law of thermodynamics. Both the dissipation rate and the time derivative of the Gibbs free energy can be split into two contributions, one due to the isomerization steps ($T\dot{\Sigma}_{iso}$), and the other to the self-assembly steps ($T\dot{\Sigma}_{sa}$):

$$T\dot{\Sigma} = T\dot{\Sigma}_{sa} + T\dot{\Sigma}_{iso}$$
$$d_t G = d_t G_{sa} + d_t G_{iso}$$

5.3.1 Energy dissipation

The part of the absorbed power which is dissipated by the self-assembly steps is calculated as:

$$T\dot{\Sigma}_{sa} = -(v_1 \Delta\mu_1 + v_3 \Delta\mu_3)$$

At the stationary state, since the Gibbs free energy is a state function, all the power absorbed by system is dissipated to sustain the non-equilibrium condition ($d_t G = 0$):

$$\dot{W}_{h\nu} = T\dot{\Sigma} = T\dot{\Sigma}_{sa} + T\dot{\Sigma}_{iso}$$

with $T\dot{\Sigma}_{iso} = \dot{W}_{h\nu} - T\dot{\Sigma}_{sa} \geq 0$. The above equation allows for the following thermodynamic interpretation. At the steady state, to maintain the free energy storage, that is keeping the self-assembly reactions away from equilibrium ($T\dot{\Sigma}_{sa} > 0$), part of the power absorbed by the photoisomerization steps ($\dot{W}_{h\nu}$) needs to be transferred to the self-assembly ones, allowing them to dissipate.

This means that the supramolecular pump operates as a (thermal) engine transducing free energy from the photons to the self-assembly processes through the photoisomerization processes. Therefore, free energy storage, and consequently unidirectional motion of the ring-axle pairs, are sustained by light energy absorption.

At the steady state $v_1 = -v_3 = v_{cy}$, thus $T\dot{\Sigma}_{sa} = -v_{cy}(\Delta\mu_1 - \Delta\mu_3)$. Upon integration of this equation over the time it takes for a mole of rings to complete one cycle ($\tau_{cy} = 1/v_{cy}V$) and multiplying by the volume, we find that the free energy dissipated by the motor per cycle of operation at the steady state reported in the main text is given by:

$$T\Delta_{cy}\Sigma_{sa} = -(\Delta\mu_1 - \Delta\mu_3)$$

In turns, this value also sets a limit to the amount of work which self-assembly steps can perform per mole of rings which complete one pumping cycle.

5.3.2 Energy storage

The free energy density stored in the self-assembly steps at steady state can be defined by virtue of the timescale separation between the relaxation times of the self-assembly steps and the isomerization ones. In fact, once the photon flow is stopped, the self-assembly steps reach their (local) equilibrium much faster than the isomerization reactions, which can equilibrate only via the very slow thermal relaxation steps. Therefore, the relative amounts of *E* and *Z* species are preserved. In these conditions, the free energy released by the relaxation to equilibrium of the self-assembly steps alone corresponds to the fraction of free energy they stored. In the following the suffix “dark” indicates that the quantity is referred to the local equilibrium, while the other quantities are considered at the dissipative steady state. The following mass balances hold true upon relaxation to the local equilibrium:

$$[EC] + [E] = [EC]_{dark} + [E]_{dark}$$
$$[ZC] + [Z] = [ZC]_{dark} + [Z]_{dark}$$
$$[EC] + [ZC] + [C] = [EC]_{dark} + [ZC]_{dark} + [C]_{dark}$$

Moreover, for the concentration at local equilibrium (in dark) the following relations hold true:

$$K_E = \frac{k_1}{k_{-1}} = \frac{[EC]_{dark}}{[E]_{dark}[C]_{dark}}$$
$$K_Z = \frac{k_3}{k_{-3}} = \frac{[ZC]_{dark}}{[Z]_{dark}[C]_{dark}}$$

With the above five equations, we can uniquely compute the (local) equilibrium concentrations ($[i]_{dark}$) by just knowing the steady state concentration in an experimental regime and the in/out kinetic rate constants of the self-assembly steps. The free energy stored in the self-assembly steps per unit volume at the steady state reached in any experimental regime as reported in the main text can then be computed as:

$$\Delta G_{sa} = G - G_{dark}$$

Since the Gibbs free energy of the system per unit of volume is $G = \sum_i [i](\mu_i - RT)$, then the stored energy density becomes:[9]

$$\Delta G_{sa} = \sum_i [i](\mu_i - RT) - [i]_{dark}\left(\mu_{i,dark} - RT\right) = RT \sum_i [i] \ln \frac{[i]}{[i]_{dark}} - [i] + [i]_{dark}$$

which was used to calculate the energy storage reported in the main text.

5.4 Energy Transduction Efficiency

The efficiency at which the motor, at steady state, converts the light energy into chemical energy available to the self-assembly reactions can be defined in two ways. The first, reported in the main text (η), consists in evaluating the fraction of work performed by the radiation (free energy) on the system which is successfully transferred to the self-assembly steps:

$$\eta = \frac{T\dot{\Sigma}_{sa}}{\dot{W}_{h\nu}}$$

This quantity is bounded between 0 and 1 and, being based on the free energy gradient generated by the radiation ($\langle \mu_{h\nu} \rangle$), can be directly compared between different motors regardless of the provided fuel. For example, the same quantity computed for a chemically driven rotary motor results to be 5 orders of magnitude lower.[10] This can be explained by considering that the chemically driven rotary motor synthetized by the Leigh group works by transducing free energy only in form of information, while here $T\Delta_{cy}\Sigma_{sa}$ also have an energetic component due to the energy ratchet mechanism.

Additionally, in the spirit of Carnot's efficiency of thermal machines, we can evaluate the ratio between the free energy transduced to the self-assembly steps per unit time and unit volume (dissipation $T\dot{\Sigma}_{sa}$), and the heat absorbed from the radiation (the hot reservoir) per unit time and unit volume ($\dot{Q}_{h\nu}$), according to the following equation:

$$\eta_2 = \frac{T\dot{\Sigma}_{sa}}{\dot{Q}_{h\nu}} \leq \langle \eta_C \rangle$$

Where $\dot{Q}_{h\nu} = \frac{N_A hc}{\lambda V} q_{n,p}\left(1 - 10^{-b\sum_i \varepsilon_i[i]}\right)$ is the total power absorbed by the sample in the unit time and volume. The fact that this efficiency is upper limited by the average Carnot efficiency (proof in section 5.4.1) makes η_2 an interesting quantity to understand how close the motor, seen as a thermal engine, works to the theoretical limit imposed by Carnot efficiency. The comparison is done in Table S8, which shows that at best this motor reaches 0.04% of Carnot efficiency and decreases with the photon flow. All the considerations in the main text aimed at rationalizing the trend of the energy transduction efficiency (η) hold for the Carnot-like efficiency η_2.

Table S8. Ratio between the average Carnot-like and Carnot's efficiency ($\eta_2/\langle\eta_C\rangle$) at the investigated photon flows.

	$q_{n,p}$ (Einstein s^{-1})			
	4.4×10^{-9}	**1.1×10^{-8}**	**2.2×10^{-8}**	**4.4×10^{-8}**
$\eta_2/\langle\eta_C\rangle$ **(%)**	0.04	0.03	0.02	0.01

5.4.1 Proof of the bound $\eta_2 \leq \langle\eta_C\rangle$

Consider the following expression of the Second Law of thermodynamics as it applies for the system under study inside a volume element $dV_{cyl}(r)$ at the steady state:

$$T\dot{\Sigma}(r) = T\dot{\Sigma}_{iso}(r) + T\dot{\Sigma}_{sa} = \frac{d\dot{W}(r)}{dV_{cyl}(r)} - T\dot{\Sigma}_{sa} + T\dot{\Sigma}_{sa} = \dot{Q}_{h\nu}(r)\eta_C(r) - T\dot{\Sigma}_{sa} + T\dot{\Sigma}_{sa} \geq 0$$

where $T\dot{\Sigma}_{iso}(r)$ and $T\dot{\Sigma}_{sa}$ are both positive quantities and $\dot{Q}_{h\nu}(r) = N_A h\nu \frac{dq_{n,p}(r)}{dV_{cyl}(r)}$ is the heat per unit volume which is absorbed by the system in the volume element. Note that $T\dot{\Sigma}_{sa}$ does not depend on r due to the homogeneity in concentrations. From the above equation follows that:

$$0 \leq \underbrace{\frac{T\dot{\Sigma}_{sa}}{\dot{Q}_{h\nu}(r)\eta_C(r)}}_{\eta} = 1 - \frac{T\dot{\Sigma}_{iso}(r)}{\dot{Q}_{h\nu}(r)\eta_C(r)} \leq 1$$

and therefore $\eta_2(r) \leq \eta_C(r)$, with $\eta_2(r) = \frac{T\dot{\Sigma}_{sa}}{\dot{Q}_{h\nu}(r)}$.

By averaging over the entire system (see section 5.2) we have:

$$\langle \eta_2 \rangle = T\dot{\Sigma}_{sa} \langle \frac{1}{\dot{Q}_{h\nu}} \rangle \leq \langle \eta_C \rangle$$

And by virtue of the inequality holding between the harmonic and the arithmetic mean of a positive defined function, we have that:

$$\langle \frac{1}{\dot{Q}_{h\nu}} \rangle \geq \frac{1}{\langle \dot{Q}_{h\nu} \rangle} \equiv \frac{1}{\dot{Q}_{h\nu}}$$

and therefore $T\dot{\Sigma}_{sa} \langle \frac{1}{\dot{Q}_{h\nu}} \rangle \geq \frac{T\dot{\Sigma}_{sa}}{\langle \dot{Q}_{h\nu} \rangle} = \frac{T\dot{\Sigma}_{sa}}{\dot{Q}_{h\nu}} = \eta_2$, which proves the inequality $\eta_2 \leq \langle \eta_C \rangle$.

7. References

1 Corra, S., Casimiro, L., Baroncini, M., Groppi, J., La Rosa, M., Tranfić Bakić, M., Silvi, S. & Credi, A. Artificial Supramolecular Pumps Powered by Light. *Chem. Eur. J.* **27**, 11076–11083 (2021).

2 L. Vetráková, V. Ladányi, J. A. Anshori, P. Dvořák, J. Wirz, D. Heger The Absorption Spectrum of cis-Azobenzene. *Photochem. Photobiol. Sci.* **16**, 1749–1756 (2017).

3 V. Ladányi, P. Dvořák, J. A. Anshori, L. Vetráková, J. Wirz, D. Heger Azobenzene Photoisomerization Quantum Yields in Methanol Redetermined. *Photochem. Photobiol. Sci.* **16**, 1757–1761 (2017).

4 Astumian, R. D. & Bier, M. Mechanochemical Coupling of the Motion of Molecular Motors to ATP Hydrolysis. *Biophys. J.* **70**, 637-653 (1996).

5 Onsager, L. Reciprocal Relations in Irreversible Processes. I. *Phys. Rev.* **37**, 405–426 (1931).

6 Mauser, H. & Gauglitz, G. *Photokinetics: theoretical fundamentals and applications* (Elsevier, 1998).

7 Demirel, Y. & Gerbaud, V. Chapter 8: Chemical Reactions. *Nonequilibrium Thermodynamics Transport and Rate Processes in Physical, Chemical and Biological Systems* (Elsevier, 2019).

8 a) Ries, H. & McEvoy, A. J. Chemical Potential and Temperature of Light. *J. Photochem. Photobiol. A* **59**, 11–18 (1991); b) Gräber, P. & Milazzo, G. *Bioenergetics* (Birkhäuser, 1997); c) P. Würfel, P. & Würfel, U. *Physics of Solar Cells: From Basic Principles to Advanced Concepts* (Wiley-VCH, 2016); d) Penocchio, E., Rao, R. & Esposito, M. Nonequilibrium Thermodynamics of Light-Induced Reactions. *J. Chem. Phys.* **155**, 114101 (2021).

9 The relation is obtained by considering that $\sum_i [i]_{dark} \mu_{i,dark} = \sum_i [i] \mu_{i,dark}$, which can be proven *via* chemical reaction network techniques by noticing that the vector with elements $\mu_{i,dark}$ is a left-null vector of the stoichiometric matrix when only self-assembly steps are considered.

10 a) Wilson, M. R., Sola, J., Carlone, A., Goldup, S. M., Lebrasseur, N. & Leigh, D. A. An Autonomous Chemically Fueled Small-Molecule Motor. *Nature* **534**, 235-240 (2016); b) Amano, S., Esposito, M. Kreidt, E., Leigh, D. A., Penocchio, E. & Roberts, B. M. W. Insights from an Information Thermodynamics Analysis of a Synthetic Molecular Motor. *Nat. Chem.* (2022) doi: 10.1038/s41557-022-00899-z.